REDUCED ORDER HOMOGENIZATION MODELS FOR FAILURE OF HETEROGENEOUS MATERIALS

By

Paul Anthony Sparks

Dissertation

Submitted to the Faculty of the

Graduate School of Vanderbilt University

in partial fulfillment of the requirements

for the degree of

DOCTOR OF PHILOSOPHY

in

Civil Engineering

May, 2015

Nashville, Tennessee

Approved:

Caglar Oskay, Ph.D

Prodyot Basu, Ph.D

Sankaran Mahadevan, Ph.D

Haoxiang Luo, Ph.D

For David and Juanita Sparks (Daddy and Mommy)

ACKNOWLEDGMENTS

I would like to express my greatest gratitude to my advisor Dr. Caglar Oskay. I initially did not want to pursue a PhD but my advisor seen something in me and gave me a chance to be a part of his research group. Through his guidance, I was able to strengthen my computational mechanics background and accomplish my research.

I would also like to thank Dr. Basu, my research father, he watched me closely every step of the way at Vanderbilt from undergraduate to graduate school. Without his guidance and support, I would have been lost.

I would like to thank my Ph.D. committee members Dr. Sankaran Mahadevan and Dr. Haoxiang Luo, for their support, encouragement and advice.

I would like to thank Dr. Robert Crouch for his support, encouragement, advice, friendship and all around knowledge that he has shared with me and took the time to pour into me and help to bolster my understanding.

I also want to thank my current and former research group members Dr. Tong Hui, Dr. Hao Yan, Matthew Pike, Michael Bogdanor, Shuhai Zhang, Xiang Zhang, Rudraprasad Bhattacharyya, Ruize Hu, Scott Williams, and Lizzie Young, for their help and friendship.

Most importantly, I would like to thank my wonderful parents (David and Juanita) for their eternal love and support. Also, to the Sparks family the original 13 children (Michael, Benjamin, Joseph, Moses, Daniel, Keturah, Lydia, Dr. Sharon, Lois, Timothy, Jonathan, and Stephen. To my many aunts, uncles, cousins, nieces and nephews, I love you guys and thanks for your support!

To my beautiful wife, my heart, and my better half, Severine and my daughter Kylina Valentine Sparks I love you guys and thanks for reminding me every day of what is important in life!

I would like to thank Jeremy Cato for always being there for me and being a great friend. To my Beecher Bee's, my Jean Child Young Wolf Pack members, all the way to

my Benjamin E. Mays High Raiders and finally to my Vanderbilt community and family, thanks!

There are scores of people who I am not able to name but I am thankful for your support and helping me to achieve my goal.

Finally, I acknowledge the financial and technical support from the Southern Regional Education Board and Vanderbilt University. Praises be to the Most High!

TABLE OF CONTENTS

LIST OF FIGURES

Chapter 1

INTRODUCTION

1.1 Motivation

Quality research involving advanced materials, particularly composite materials, has provided solutions to challenges faced across several industries, including aerospace and automotive. The syntheses of these composite materials are usually superior in their performance due to the combination of the different interactions between their material properties and chemical compositions. Not only have these material innovations led to technological breakthroughs in new engineering structures, (i.e., stronger and lighter comparatively than traditional metallic materials) but engineering design tools have steadily complimented these advancements.

Advances in computational power have allowed researchers to develop a strong computational framework, which can model and simulate the failure process of these composite materials. These new materials span a broad range of length scales, thus they exhibit a rich variety of microstructures with varying degrees of disorder (i.e., material heterogeneities). Therefore, questions concerning their quantitative characterizations continue to present many fundamental and practical challenges.

Shortcomings of this field included the need to accurately model the microstructure of the composite material and characterize its varying length scales. The size scale difference between the scale of the overall composite material and the constituent materials where failure initiates and propagates exists and is an issue. Therefore, massive amounts of computational power would be required to accurately resolve the microstructures of these composite materials and would be computationally formidable to complete the analysis. The lack of sufficient experimental data has made it difficult to characterize the performance of

these advanced composite materials. Lastly, a wide variety of failure mechanisms acting on microstructures of the composite materials has led to problems predicting the behavior of the material.

From the academic front, several numerical theories have been developed to predict the behavior of these composite materials. One methodology of interest is computational homogenization, which has emerged as a powerful modeling and simulation tool for structures made of composite and heterogeneous materials. The key characteristic of computational homogenization is that the macroscopic constitutive behavior of the heterogeneous material is provided by the numerical solution of a boundary value problem defined over the representative volume of the microstructure. One of the main challenges of computational homogenization is the computational complexity involved in solving boundary value problems at two (or more) scales.

Eigendeformation-based reduced order homogenization method has been shown to be an effective approach to significantly improving the computational efficiency of computational homogenization while maintaining reasonable accuracy. The methodology can be applied to problems involving material nonlinearities [1, 2, 3], as well as interface decohesion at the microstructural scale [4, 5]. This approach employs the transformation field analysis [6, 7], and evaluates the nonlinear microscale problem using only a small set of unknowns through construction of microstructural influence functions and localization operators that are pre-computed using linear elastic microscale problems. Many reduced order approaches rely on representing the nonlinear response using a small number of functions, spanning a basis with dimensions much smaller than the full scale microscale boundary value problem. Choosing the appropriate basis, as well as choosing the model order that can represent the fine scale response, is therefore a critical question. The basis functions are typically reduced from the response of fully resolved microstructure problems subjected to a small number of load scenarios that the overall structure is expected to undergo. In nonlinear problems, the microstructure loading may significantly change through the course of

the loading due to load redistribution. While the reduced order models are accurate in the load conditions at which they are derived, their performance at full load spectrum is not always accurate.

Predictive failure models in continuum damage mechanics have been an area of interest because multifaceted failure mechanisms can occur due to the complex interactions between the microconstituents. Different failure mechanisms include fiber buckling, fiber fracture, matrix failure and fiber matrix debonding [8]. Advances in computational algorithms have allowed researchers to develop a strong computational framework which is able to model and simulate the failure process of composite materials.

The fundamental focus of this dissertation is to draw attention to the development of practical domain partitioning strategies to reduce the computational cost within the multiscale eigendeformation-based reduced order homogenization framework. This dissertation addresses four major issues: (i) integrating multiscale computational homogenization using eigendeformation-based reduced order homogenization [1, 2, 3] within a search heuristic framework (i.e., genetic algorithms). This approach mimics natural selection to identify the optimal reduced order basis for inelastic and failure response within heterogeneous materials. (ii) To reduce the computational cost of the existing multiscale methodologies, these potential crack failure paths are allowed to overlap and the collections of these parts will characterize the domain of the proposed ROM, further reducing the number of internal state variables in the model. This ideas utilize the basic principles of combinatorics [9, 10, 11]. (iii) Provide an alternative to the methodology proposed by Fish and co-workers [12], where the inclusion locking phenomenon leads to spurious post failure residual stresses. (iv) Lastly, to extend the applicability of overlapping failure paths to more complex microstructures in three dimensions addressing the issues of computational cost when evaluating large, realistic structural domains.

1.2 Research Objectives & Tasks

This dissertation presents a reduced order multiscale methodology to simulate and predict failure in heterogeneous materials. The research objectives stated below were aligned to provide the basis for ongoing work in the development of a new multiscale tool useful for simulating failure in composites within aerospace applications. The primary research objectives for my dissertation are as follows:

1. Create a reduced order multiscale methodology for the simulation of failure in brittle composite structures which operates in a heuristic framework.

2. Create an efficient and accurate methodology which saves computational effort when evaluating the reduced order models, alleviates mesh dependency of multiscale modeling, and addresses residual stress locking post failure in the composite materials.

3. Apply the new reduced order methodology to life prediction in brittle composite materials by conducting numerical experimental investigations.

The proposed reduced order modeling methodology is implemented to model the brittle response of the composite material. The matrix material of the composite structure is subjected to various loading modes and the failure of the matrix material is the foundation for the selection of the ROM basis.

1.3 Dissertation Organization

The first research objective was addressed by the identification of the optimal reduced order model which the details are discussed in Chapter 2. The identification of the optimal reduced order model is posed as an integer optimization problem and the genetic algorithm is used to evaluate the fitness of every individual within the population after a series of successive events [i.e., selection of individuals, cross-over, mutation, and population generation]. This elite individual, not only satisfies optimality, but has the best genetic coding

(elemental genes) which can be used as the partition for the evaluation of the reduced order model. The identification of the optimal ROM validates the method of failure paths. The optimal ROM is verified against direct numerical simulations of a heterogeneous particle reinforced material. In Chapter 3, the reduced order model is improved. The accuracy and computational efficiency of the reduced order model is related to the number of parts forming a partition for a specific reduced model order, n. As the number of parts increases for a particular reduced model order, the computational complexity increases and ultimately results in a larger set of nonlinear equations that must be evaluated. This issue is overcome by allowing the potential crack paths to overlap which reduces the number of internal state variables that characterizes the ROM. The reduced order model does not capture the post-failure response of the representative volume element accurately. To address this issue of inclusion locking, new sets of coefficient tensors are generated to exhibit a near 'zero' mode in the reduced order coarse-scale stress computation. The details are discussed in Chapter 3. Since each chapter contains related but separate topics, an introduction to each chapter provides a review of the relevant literature. Finally, Chapter 4 contains conclusions and future research.

Chapter 2

IDENTIFICATION OF OPTIMAL REDUCED ORDER HOMOGENIZATION MODELS FOR FAILURE OF HETEROGENEOUS MATERIALS

2.1 Introduction

Computational homogenization is emerging as a powerful modeling and simulation tool for structures made of composite and heterogeneous materials. The computational homogenization method is based on the mathematical homogenization theory pioneered by Babuska [13], Bensoussan [14], Suquet [15], and Sanchez-Palencia [16]. The key characteristic of this method is that the macroscopic constitutive behavior of the heterogeneous material is provided by the numerical solution of a boundary value problem defined over the representative volume of the microstructure. The computational homogenization method has been successfully applied to evaluate the mechanical and functional behavior of materials with complex microstructures that include inelastic, viscous and damage effects [17, 18], geometric nonlinearities [19, 20] and multiphysics response [21, 22]. Recently, significant research is ongoing to extend the computational homogenization approach to model failure and cracking phenomena in composite materials [23, 24, 25].

One of the main challenges of computational homogenization is the computational complexity involved in solving boundary value problems at two (or more) scales. The issue of computational complexity is addressed using parallel implementation strategies, reduced order modeling at the coarse scale using high order (i.e., plate and shell) theories or reduced order modeling at the fine scales to efficiently evaluate the microscale response, as well as a combination of these three approaches. Parallelization of the computational homogenization [24, 26, 27] is natural and domain decomposition is readily applicable due to the local character of the microscale boundary value problems that are typically evalu-

ated at the integration points of the macroscale grid. Model reduction at the coarse scale is achieved by exploiting the characteristics of the macroscopic domain. For instance, plate and shell theories have been recently employed to evaluate the response of thin structures with heterogeneous microstructure [28, 29, 30, 31].

The third approach to reducing the computational cost of the computational homogenization method is to approximate the microscale boundary value problem with a reduced order representation. This approach finds its roots in the effective medium theory [32], which provides analytical or semi-analytical approximation to the microscale problem. More recently, computational reduced order models have been proposed to address complex microstructural topologies and nonlinear behavior. Major progress in reduced order modeling has been made using the boundary element method [33], the Voronoi cell method [34], the method of cells [35], the fast Fourier transforms [36], the network approximation method [37], the proper orthogonal decomposition [38] and the proper generalized decomposition [39]. Eigendeformation-based reduced order homogenization method has been shown to be another effective approach that can be applied to problems involving material nonlinearities [1, 2, 3], as well as interface decohesion at the microstructural scale [4, 5]. This approach employs the transformation field analysis [6, 7] and evaluates the nonlinear microscale problem using only a small set of unknowns through construction of microstructural influence functions and localization operators that are pre-computed using linear elastic microscale problems. Many reduced order approaches rely on representing the nonlinear response using a small number of functions spanning a basis with dimensions much smaller than the full scale microscale boundary value problem. Choosing the appropriate basis, as well as the order that can represent the fine scale response is therefore the critical question. The basis functions are typically reduced from the response of fully resolved microstructure problems subjected to a small number of load scenarios that the overall structure is expected to undergo. In nonlinear problems, the microstructure loading may significantly change through the course of the loading due to load redistribution. While

the reduced order models are accurate in the load conditions at which they are derived, their performance at full load spectrum is not always accurate.

In this chapter, a methodology to identify optimal reduced order homogenization models for efficiently approximating the inelastic and failure response of heterogeneous materials is provided. The reduced order modeling approach taken in this study is the eigendeformation-based reduced order homogenization method [4]. The identification of the optimal reduced order model lends itself as an integer optimization problem, which is evaluated using the genetic algorithm optimization technique. In particular, this chapter addresses (1) how to identify the best reduced order basis for a given model order; (2) the effect of increasing the model order on the overall accuracy of the microscale computations; and, (3) the accuracy characteristics of the optimal reduced order models across a full load spectra beyond the loading directions at which the reduced order models are developed.

The remainder of this chapter is organized as follows: The macroscale and microscale problems in the context of the computational homogenization method are described in Section 2.2. Section 2.3 provides the reduced order model based on the eigendeformation-based reduced order homogenization method. In Section 2.4, the problem statement for the identification of the optimal reduced order model is provided. The solution methodology based on genetic algorithm and the details of the implementation of the identification problem is described. The numerical examples are discussed in Section 2.5.

2.2 Computational Homogenization

The inelastic deformation in the macroscopic domain, Ω, are modeled with a heterogeneous microstructure as illustrated in Fig. 2.1. The domain of the representative microstructure, Θ, consists of $c \geq 2$ constituent phases. The macroscopic domain is formed by the repetition of the microstructure. The macroscopic and microscopic domains are parameterized by the position vectors, $\mathbf{x}$ and $\mathbf{y}$, respectively. The response fields (e.g., displacement, strain, stress) are taken to be periodic with respect to Θ. The macro- and microscale po-

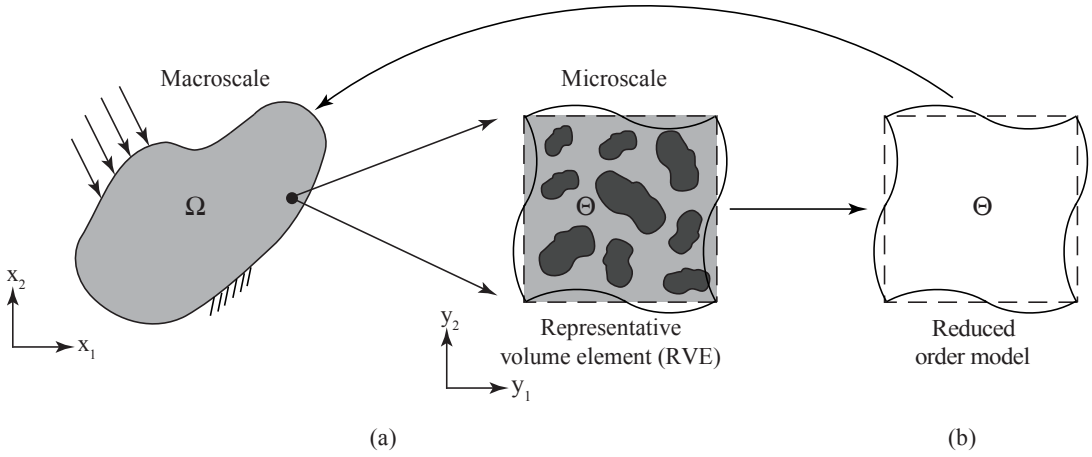

Figure 2.1: Macro- and microscopic structures.

sition vectors are related by the small positive scaling parameter ζ (i.e., $0 < \zeta \ll 1$), such that $\mathbf{y} = \mathbf{x}/\zeta$.

The mathematical homogenization theory with multiple scales [14] is employed to formulate coupled boundary value problems that describe the response of an equivalent homogeneous domain (i.e., the macroscale problem) and the representative volume element (i.e., the microscale problem). To this extent, the displacement field is decomposed using a two-scale asymptotic expansion:

$$u_i(\mathbf{x},\mathbf{y},t) = \bar{u}_i(\mathbf{x},t) + \zeta u_i^1(\mathbf{x},\mathbf{y},t) \tag{2.1}$$

in which, $\bar{u}_i$ and u_i^1 are the macroscopic and microscopic displacement fields, respectively. The two-scale decomposition of the displacement field is substituted in the governing equations of equilibrium and asymptotic analysis is employed to decompose the governing equations into the macro- and microscale counterparts [4].

2.2.1 Macroscale problem

Applying the two-scale asymptotic decomposition into the equilibrium equations, considering the $O(1)$ terms and averaging over the representative volume element (RVE) leads

to the following macroscale equilibrium equation defined over the macroscopic domain, Ω:

$$\bar{\sigma}_{ij,x_j}(\mathbf{x},t) + \bar{b}_i(\mathbf{x},t) = 0 \tag{2.2}$$

in which, $\bar{\sigma}_{ij}$ and $\bar{b}_i$ denote the macroscopic stress tensor and body force, respectively, which are volume-averaged over the domain of the RVE, Θ:

$$\bar{\sigma}_{ij}(\mathbf{x},t) = \left\langle \sigma_{ij} \right\rangle \tag{2.3}$$

$$\bar{b}_i(\mathbf{x},t) = \langle b_i \rangle \tag{2.4}$$

where, the Macaulay brackets are defined as:

$$\langle \cdot \rangle = \frac{1}{|\Theta|} \int_{\Theta} (\cdot) d\mathbf{y} \tag{2.5}$$

$|\Theta|$ is the volume of the RVE.

The stress field is expressed as:

$$\sigma_{ij}(\mathbf{x},\mathbf{y},t) = L_{ijkl}(\mathbf{y}) \left[\bar{\varepsilon}_{kl}(\mathbf{x},t) + u^1_{(k,y_l)}(\mathbf{x},\mathbf{y},t) - \mu_{kl}(\mathbf{x},\mathbf{y},t) \right] \tag{2.6}$$

where, L_{ijkl} is the fourth order tensor of elastic moduli that vary within the RVE due to material heterogeneity. L_{ijkl} is taken to be symmetric and strongly elliptic. $\bar{\varepsilon}_{ij} = \bar{u}_{(i,x_j)}$ is the macroscopic strain tensor; a subscript comma denotes differentiation, parentheses in the subscript denotes a symmetric differentiation. Small strain kinematics with additive split of the strain tensor is assumed: $\varepsilon_{ij} = \varepsilon^e_{ij} - \mu_{ij}$, where ε^e_{ij} is the elastic strain and μ_{ij} is the history-dependent inelastic strain tensor present due to one or a combination of plastic, viscous, damage and thermal processes, described in terms of internal state variables. In this section, the inelastic processes are modeled using a scalar continuum damage mechanics model for simplicity. The evolution equations for the damage model are explained below.

The boundary conditions of the macroscale problem are defined as:

$$\bar{u}_i(\mathbf{x},t) = g_i(\mathbf{x},t); \quad \mathbf{x} \in \Gamma_u \tag{2.7}$$

$$\bar{\sigma}_{ij}(\mathbf{x},t)\, n_j = t_i(\mathbf{x},t); \quad \mathbf{x} \in \Gamma_t \tag{2.8}$$

in which, g_i is the boundary displacement data prescribed on $\Gamma_u \subset \partial\Omega$; and, t_i is the boundary traction data prescribed on $\Gamma_t \subset \partial\Omega$, such that $\Gamma_u \cap \Gamma_t = \emptyset$ and $\Gamma_u \cup \Gamma_t = \partial\Omega$. The prescribed boundary conditions are taken to vary with respect to the macroscopic scale only and are constant with respect to the microscopic coordinates.

2.2.2 Microscale problem

Applying the two-scale asymptotic decomposition into the equilibrium equations, considering the $O(\zeta^{-1})$ terms leads to the following microscale equilibrium equation defined over the RVE domain, Θ:

$$\sigma_{ij,y_j}(\mathbf{x},\mathbf{y},t) = 0 \tag{2.9}$$

where, σ_{ij} is given in Eq. 2.6. Equation 2.9 is evaluated for the microscale displacement field, u_i^1, where the macroscopic strain, $\bar{\varepsilon}_{ij}$ acts as the loading function for the microscale problem. The boundary condition of the microscale problem is taken to be periodic. For a rectangular cuboidal shaped RVE domain, the boundary is split into n_{sd} subdomains denoted by Γ_ξ, where $n_{\text{sd}} = 2$ or 3 is the number of spatial dimensions. Each boundary subdomain is a pair of parallel faces of the RVE boundary. The periodic boundary conditions are expressed as:

$$u_i^1(\mathbf{y},t) = u_i^1\left(\mathbf{y} - l_\zeta \mathbf{n}_\xi, t\right); \quad \mathbf{y} \in \Gamma_\xi; \quad \xi = 1,\ldots,n_{\text{sd}} \tag{2.10}$$

in which, $\mathbf{n}_\xi$ is the unit outward normal on Γ_ξ, and l_ξ is the length of the RVE along $\mathbf{n}_\xi$. Zero microscale displacement is imposed at the vertices of the RVE domain to restrict rigid

body motion.

2.3 Reduced Order Homogenization

When solving linear problems, the linearity of the microscale displacement field with respect to the macroscopic strains is exploited to pose the microscale problem in terms of a third order influence function, H_{ikl} (i.e., $u_i^1(\mathbf{x},\mathbf{y}) = H_{ikl}(\mathbf{y})\,\bar{\varepsilon}_{kl}(\mathbf{x})$). The macroscale stress is then a function of H_{ikl}. The influence function is computed numerically and then employed in the evaluation of the macroscale problem. In nonlinear problems, the microscale displacement field is a nonlinear and typically history-dependent function of the macroscale strain field. Therefore, a separate microscale problem is assigned to each integration point of a macroscale problem and evaluated for every load increment and iteration of a macroscale analysis. The computational burden in this approach is tremendous in case of large structural simulations or when the microstructure is complex. The eigendeformation-based reduced order homogenization approach [4, 5] was employed to develop a reduced order model for efficiently solving for the microscale response. The microscopic displacement field is expressed as:

$$u_i^1(\mathbf{x},\mathbf{y},t) = H_{ikl}(\mathbf{y})\,\bar{\varepsilon}_{kl}(\mathbf{x},t) + \int_\Theta h_{ikl}(\mathbf{y},\hat{\mathbf{y}})\,\mu_{kl}(\mathbf{x},\hat{\mathbf{y}},t)\,d\hat{\mathbf{y}} \tag{2.11}$$

$$u_i^1(\mathbf{x},\mathbf{y},t) = H_{ikl}(\mathbf{y})\,\bar{\varepsilon}_{kl}(\mathbf{x},t) + \tilde{u}_i(\mathbf{x},\mathbf{y},t) \tag{2.12}$$

$$\tilde{u}_i(\mathbf{x},\mathbf{y},t) = \int_\Theta h_{ikl}^{ph}(\mathbf{y},\hat{\mathbf{y}})\,\mu_{kl}(\mathbf{x},\hat{\mathbf{y}},t)\,d\hat{\mathbf{y}} \tag{2.13}$$

The inelastic influence function, h_{ikl}, consists of the particular solutions of the RVE and is approximated by numerical solutions of the linear elastic RVE problems [4]. The inelastic strain field is expressed as:

$$\mu_{ij}(\mathbf{x},\mathbf{y},t) = \sum_{\alpha=1}^{n} N^{(\alpha)}(\mathbf{y})\,\mu_{ij}^{(\alpha)}(\mathbf{x},t) \tag{2.14}$$

$$\mu_{ij}(\mathbf{x},\mathbf{y},t) = \sum_{\gamma=1}^{n} N^{(\gamma)}(\mathbf{y})\,\mu_{ij}^{(\gamma)}(\mathbf{x},t) \tag{2.15}$$

where, $N^{(\alpha)}$ are the mesomechanical shape functions; n is the order of discretization (also referred to as the model order in this section), and $\mu_{ij}^{(\alpha)}$ are the microscopically nonlocal inelastic strain coefficients:

$$\mu_{ij}^{(\alpha)}(\mathbf{x},t) = \int_{\Theta} \varphi^{(\alpha)}(\mathbf{y})\,\mu_{ij}(\mathbf{x},\mathbf{y},t)\,d\mathbf{y} \tag{2.16}$$

$$\mu_{ij}^{(\gamma)}(\mathbf{x},t) = \int_{\Theta} \varphi^{(\gamma)}(\mathbf{y})\,\mu_{ij}(\mathbf{x},\mathbf{y},t)\,d\mathbf{y} \tag{2.17}$$

in which, $\varphi^{(\alpha)}$ are mesomechanical weight functions. Employing Eqs. 2.13, 2.15, and 2.1, a kinematic relationship between the nonlocal inelastic strain coefficients and nonlocal total strain coefficient is obtained:

$$\varepsilon_{ij}^{(\gamma)}(\mathbf{x},t) = A_{ijkl}^{(\gamma)}\bar{\varepsilon}(\mathbf{x},t) + \sum_{\beta=1}^{n} P_{ijkl}^{(\gamma\beta)}\mu_{kl}^{(\beta)}(\mathbf{x},t) \tag{2.18}$$

where, $\varepsilon_{ij}^{(\alpha)}$ is defined analogous to Eq. 2.17, and:

$$A_{ijkl}^{(\gamma)} = I_{ijkl} + \int_{\Theta} \varphi^{(\gamma)}(\mathbf{y})\,G_{ijkl}(\mathbf{y})\,d\mathbf{y} \tag{2.19}$$

$$P_{ijkl}^{(\gamma\beta)} = \int_{\Theta}\int_{\Theta} \varphi^{(\gamma)}(\mathbf{y})\,g_{ijkl}(\mathbf{y},\hat{\mathbf{y}})\,N^{(\beta)}(\hat{\mathbf{y}})\,d\hat{\mathbf{y}}d\mathbf{y} \tag{2.20}$$

in which, $G_{ijkl} = H_{(ikl,y_j)}$ and $g_{ijkl} = h_{(ikl,y_j)}$ are elastic and inelastic polarization tensors, respectively; and, I_{ijkl} the fourth order identity tensor. The evolution of the inelastic strains is modeled in terms of the nonlocal variables. In the functional form:

$$\dot{\mu}_{ij}^{(\alpha)} = f\left(\mu_{ij}^{(\alpha)}, \varepsilon_{ij}^{(\alpha)}, \sigma_{ij}^{(\alpha)}, \mathbf{h}^{(\alpha)}\right) \tag{2.21}$$

where, $\sigma_{ij}^{(\alpha)}$ is the nonlocal stress coefficients defined analogous to Eq. 2.17 and using Eq. 2.6, and $\mathbf{h}^{(\alpha)}$ denotes additional internal state variables defining the evolution of the

inelastic process. Equation 2.21 along with Eq. 2.18 are evaluated to obtain $\mu_{ij}^{(\alpha)}$ for a prescribed macroscopic strain state. The computed inelastic strain field satisfies the microscale equilibrium *a-priori* via the influence functions. The evaluation of $\mu_{ij}^{(\alpha)}$ therefore provides an approximation to the solution of the microscale problem. The specific form of the evolution equations (Eq. 2.21) requires that the nonlocal inelastic strain coefficients describe the inelastic processes at a subdomain occupied by a single constituent phase. Let $\Theta_i \subset \Theta$ denote the domain of phase i $(1 \leq i \leq c)$ within the RVE. Each phase is decomposed into n_i non-overlapping parts: $\Theta_i = \cup_{j=1}^{n_j} \Theta_i^{(j)}$, where $\Theta_i^{(j)} \cap \Theta_i^{(k)} = \emptyset$ if $j \neq k$. A part in the RVE is further defined as, $\Theta^{(\alpha)} = \Theta_i^{(j)}$ such that $\alpha = j + \sum_{k=1}^{i-1} n_k$. The mesomechanical shape and weight functions are taken to be piecewise constant within the RVE domain:

$$N^{(\gamma)}(\mathbf{y}) = \begin{cases} 1 \text{ if } \mathbf{y} \in \Theta^{(\gamma)} \\ 0 \text{ elsewhere} \end{cases} \tag{2.22}$$

$$\varphi^{(\gamma)}(\mathbf{y}) = \frac{1}{\left|\Theta^{(\gamma)}\right|} N^{(\gamma)}(\mathbf{y}) \tag{2.23}$$

where, $\left|\Theta^{(\alpha)}\right|$ is the volume of part $\Theta^{(\alpha)}$. This set of shape functions clearly forms an orthonormal basis and satisfies the partition of unity property of the reduced order basis.

2.3.1 Continuum damage mechanics model

In this study, the evolution of the inelastic strain is modeled using a scalar continuum damage mechanics model:

$$\mu_{ij}^{(\gamma)} = \omega^{(\gamma)} \varepsilon_{ij}^{(\gamma)} \tag{2.24}$$

in which, $\omega^{(\alpha)} \in [0,1)$ is the damage variable with $\omega^{(\alpha)} = 0$ and $\omega^{(\alpha)} \to 1$ indicate the states of no damage and complete loss of load carrying capacity within part $\Theta^{(\alpha)}$, respec-

tively. The evolution of the damage variable follows:

$$\omega^{(\gamma)}(\mathbf{x},t) = \Phi\left(\kappa^{(\gamma)}(\mathbf{x},t)\right); \quad \frac{\partial\Phi\left(\kappa^{(\gamma)}\right)}{\partial\kappa^{(\gamma)}} \geq 0 \tag{2.25}$$

where,

$$\kappa^{(\gamma)}(\mathbf{x},t) = \max\left\{ \upsilon^{(\gamma)}(\mathbf{x},\tau) \middle| \tau \leq t \right\} \tag{2.26}$$

$\upsilon^{(\alpha)}$ is the nonlocal damage equivalent strain defined based on the strain-based damage theory [40] as:

$$\upsilon^{(\gamma)}(\mathbf{x},t) = \sqrt{\frac{1}{2}\varepsilon_{ij}^{(\gamma)} L_{ijkl}^{(\gamma)} \varepsilon_{kl}^{(\gamma)}} \tag{2.27}$$

$L_{ijkl}^{(\alpha)}$ is the tensor of elastic moduli of the constituent phase occupying $\Theta^{(\alpha)}$. By strong ellipticity of $L_{ijkl}^{(\alpha)}$, the nonlocal damage equivalent strain is non-negative. The evolution of phase damage as a function of the phase deformation function follows the arctangent law [1]

$$\Phi^{(\gamma)} = \frac{atan\left(a^{(\gamma)}\kappa^{(\gamma)}(\mathbf{x},t) - b^{(\gamma)}\right) + atan\left(b^{(\gamma)}\right)}{\pi/2 + atan\left(b^{(\gamma)}\right)} \tag{2.28}$$

in which, $a^{(\alpha)}$ and $b^{(\beta)}$ are material parameters. Considering the particular form of the scalar damage model (Eq. 2.24), combining with Eq. 2.18 and using the shape and weight functions defined as in Eqs. 3.48 and 2.23, the nonlocal inelastic strain coefficients are expressed in the following algebraic form ($\forall\alpha = 1,2,\ldots,n$):

$$\sum_{\beta=1}^{n}\left[\delta_{\gamma\beta}I_{ijkl} - P_{ijkl}^{(\gamma\beta)}\omega^{(\gamma)}(\mathbf{x},t)\right]\mu_{kl}^{(\beta)}(\mathbf{x},t) - \omega^{(\gamma)}(\mathbf{x},t)A_{ijkl}^{(\gamma)}\bar{\varepsilon}_{kl}(\mathbf{x},t) = 0 \tag{2.29}$$

where, $\delta_{\alpha\beta}$ is Kronecker delta.

2.4 Identification of Optimal Reduced Order Model

In this section, the problem of identifying the optimal reduced order models is formulated and the solution strategy for the identification problem based on optimization with

the genetic algorithm is provided. A separate optimization problem is posed to scale the parameters of the optimal reduced order models and minimize the modeling errors.

2.4.1 Problem statement

Consider a finite element discretization of the RVE domain, $\Lambda = \{e_1, e_2, \ldots, e_{n_{\text{el}}}\}$, where e_i denotes a finite element; and, n_{el} the total number of finite elements. A reduced order model of order n is represented by an index set (i.e., individual) $X = \{X_1, X_2, \ldots, X_{n_{\text{el}}}\}$ such that $X_i = \alpha$ if $e_i \subset \Theta^{(\alpha)}$.

Let σ_{ref} and σ_X be the response metrics computed using the computational homogenization method (i.e., reference model) with full resolution of the microstructure and using the reduced order model, X of order n, respectively. The identification of the optimal reduced order model consists of minimizing the discrepancy between the response metrics computed by the reference and the reduced order models:

Find $X^* \in \chi^n \equiv \{X \,|\, 1 \leq X_i \leq n\}$, which satisfies:

$$\mathbb{F}(X^*) = \min_{X \in \chi^n} \left\| \sigma_{ref} - \sigma_X \right\|_{(\cdot)} \tag{2.30}$$

where χ^n is a set of all possible individuals that define a reduced order model with model order, n, and X^* is the optimal reduced order model. In this section, the macroscopic stress-strain response when subjected to n_{load} loading conditions are taken as the response metric. The objective function becomes:

$$\mathbb{F}(X^*) = \min_{X \in \chi^n} \sum_{\kappa=1}^{n_{load}} \left\| \bar{\sigma}_{ref}^{(\kappa)}(\bar{\varepsilon}_{ij}) - \bar{\sigma}_X^{(\kappa)}(\bar{\varepsilon}_{ij}) \right\|_2 \tag{2.31}$$

where $\|\cdot\|_2$ denotes L_2 norm, $\bar{\sigma}_{ref}^{(\kappa)}$ and $\bar{\sigma}_X^{(\kappa)}$ are the histories of the macroscopic Von-Mises stress under the load case, κ, computed using the reference model and the reduced order model, respectively.

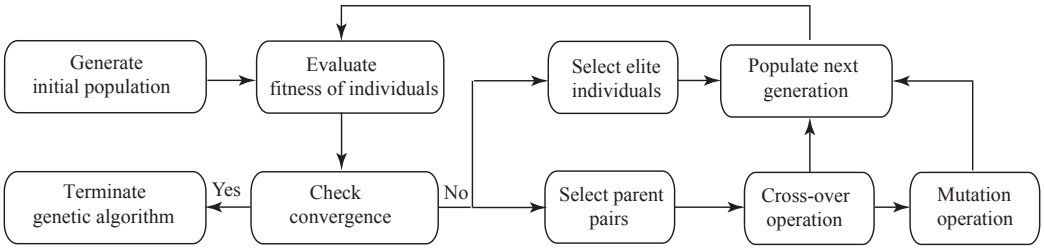

Figure 2.2: Structure of the identification strategy using genetic algorithm.

Each individual in the space χ^n represents a reduced order model of order n but the representation is non-unique: multiple individuals may represent the same reduced order model. This difficulty is alleviated by ordering of the parts, $\Theta^{(\alpha)}$. An example is the ascending order of the parts such that the element with the smallest label in each part $\Theta^{(\alpha)}$ increases with α: Let $\Lambda^{(\alpha)} = \{e_i \,|\, e_i \in \Theta^{(\alpha)}; 1 \leq i \leq n_{\text{el}}\}$ be the set of the finite elements spanning the part $\Theta^{(\alpha)}$ ordered such that $\Lambda^{(\alpha)}(i) > \Lambda^{(\alpha)}(i-1)$; $2 \leq i \leq n_{\text{el}}$. The parts are reordered such that $\Lambda^{(1)}(1) < \Lambda^{(2)}(1) < \ldots < \Lambda^{(n)}(1)$.

The model order of n is ensured by assigning at least one element to each part. By this constraint a model of order m cannot be represented by a model of a higher order $n > m$.

2.4.2 Genetic algorithm

The optimal reduced order models are identified using the genetic algorithm optimization method. Identification of the optimal reduced order model is an integer optimization problem, since each individual in the search space, χ^n, is represented using an integer set. The gradient-based optimization methods [41], commonly employed in many engineering problems, are typically for real valued problems and therefore not applicable. Evolutionary (e.g., genetic) algorithms provide an effective approach to solving nonlinear integer optimization problems [42, 43, 44], since they are based on function evaluations only (no gradient information is needed or convexity required), they are global optimizers (local minima do not necessarily compromise the solution) and represent the search space digi-

tally, naturally fitting integer representations. The literature in evolutionary algorithms is vast and they have been successfully employed in a variety of problems [45, 46, 44]. Genetic Algorithms typically consist of: (a) Creation of a set of individuals (i.e., population) by random sampling of the search space. (b) Assessment of the fitness of the individuals within the population based on objective function evaluation, where the fitness of an individual is inversely proportional to the corresponding objective function. (c) Creation of a set of new individuals from the previous population (i.e., generation) based on the fitness of the individuals. Assessment of the fitness and creation of subsequent generations are repeated until an individual with the desired fitness (i.e., the extremum of the objective function) is achieved up to the chosen tolerance.

The structure of the genetic algorithm employed in this section is illustrated in Fig. 2.2. The algorithm is initiated by creating the initial population of individuals ($P = \{X^1, X^2, \ldots, X^{n_{pop}}\}$), where X^i denotes an individual; and, n_{pop} the total number of individuals in the population. The initial population is randomly generated. The fitness of each individual in the population is computed, where the fitness is defined as the inverse of the objective function provided in Eq. 2.31.

The creation of the next generation of the population consists of several steps, namely, the selection of a number of parent pairs from the current population for the cross-over operation, the mutation of some individuals in the population, and finally, the selection of elite individuals for inclusion in the next generation. The roulette wheel algorithm is employed in the selection of the parent pairs. In the roulette wheel algorithm, each individual within the population is assigned a probability of selection that is proportional to its fitness value. The parent pairs are randomly chosen from the population based on the assigned probabilities [47, 48]. The cross-over operation consists of the generation of two offspring's from each parent pair using the integer representation (chromosome) of each individual. The chromosome of each parent is split into two parts at a randomly selected locus and the chromosome fragments are interchanged between the two parents to generate

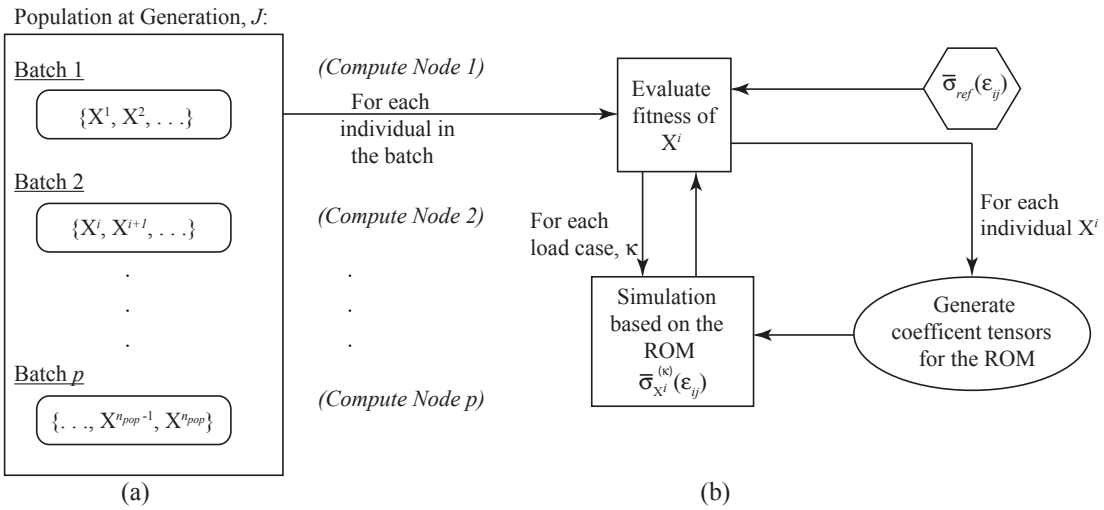

Figure 2.3: Implementation of the genetic algorithm: (a) parallel execution of the fitness evaluation; and, (b) strategy for evaluating the fitness of an individual.

two new chromosomes (the offspring's). A number of offspring's resulting from the cross-over operations are subjected to mutation, which consists of replacing a targeted gene from the chromosome of an offspring. The selection of the individual to be mutated, the gene that will be targeted and the new value of the gene are all randomly chosen. The mutation operation reduces the probability of convergence to a local minimum by including random individuals into the search space at each generation. A number of elite individuals with the highest fitness values within the populations are passed on to the next generation without change.

New generations are created until a convergence criterion is satisfied. Two convergence criteria are employed in this study. The first criterion indicates convergence when the fitness of the best individual in the current generation is less than a predefined tolerance. The second criterion indicates convergence when the change in the average fitness of the population remains under a specified tolerance for a predefined number of generations (i.e., stall generations).

The genetic algorithm optimization for the identification of the optimal reduced order model is implemented using Matlab's global optimization toolbox. The general structure

of the implementation at a given genetic algorithm step is illustrated in Figure 2.3. The genetic algorithm is implemented using a parallel solution strategy for computational efficiency. The computational cost of the identification problem is primarily due to the fitness evaluations, which consist of solving the multiscale boundary value problems. The population at a generation is split into p equal subsets (batches). The fitness of the individuals in the batches are evaluated concurrently using p compute nodes. At each fitness evaluation of an individual within a batch, the coefficient tensors for the reduced order model represented by the individual is computed. The genetic algorithm code communicates with a commercial finite element software (Abaqus) to conduct numerical simulations using the reduced order model. The user supplied subroutine functionality of Abaqus (UMAT) is used to incorporate the reduced order model into the Abaqus framework. The reference simulations based on the computational homogenization method is conducted *a-priori*, and the appropriate data is stored in a file for access during fitness computation.

2.4.3 Parameter scaling

The predictions of the reduced order models based on eigendeformation-based reduced order homogenization approach typically overestimate the strength properties. While the optimal reduced order model identification based on the methodology described above provides the best model among all possible models of the same order, the accuracy of the model can be improved by adjusting the model parameters. Let $\mathbf{s}$ be a vector of scaling constants associated with the material parameters of the microstructural constituents. The problem of identifying the parameter scaled optimal reduced order model is defined as:

Find the scaling constants, $\mathbf{s}^*$, which satisfies:

$$\mathscr{F}(\mathbf{s}^*) = \min_{s} \sum_{\kappa=1}^{n_{load}} \left\| \bar{\boldsymbol{\sigma}}_{ref}^{(\kappa)}(\bar{\boldsymbol{\varepsilon}}_{ij}) - \bar{\boldsymbol{\sigma}}_{X^*}^{(\kappa)}(\bar{\boldsymbol{\varepsilon}}_{ij};\mathbf{s}) \right\|_2 \tag{2.32}$$

where $\bar{\boldsymbol{\sigma}}_{X^*}^{(\kappa)}(\bar{\boldsymbol{\varepsilon}}_{ij};\mathbf{s})$ is the constitutive response of the optimal reduced order model using the

parameter set, $\mathbf{s}$. The identification problem constitutes nonlinear optimization with real valued parameters. Gradient based and evolutionary optimization methods are applicable in the evaluation of this problem.

The continuum damage mechanics model employed in this study includes two parameters for each microstructural constituent: $a^{(\alpha)}$ and $b^{(\alpha)}$. $a^{(\alpha)}$ controls the degree of brittleness at a material point at failure, whereas $b^{(\alpha)}$ controls the strength of the constituents. For a microstructure with two constituents (e.g., fiber and matrix), the parameter set is: $\mathbf{s} = \{s_a^{(m)}, s_b^{(m)}, s_a^{(f)}, s_b^{(f)}\}$. In the numerical examples considered in this study, the parameter scaling (Eq. 2.32) is evaluated for a single parameter $b^{(m)}$ by employing the Nelder-Mead simplex method.

2.5 Numerical Examples

Numerical verification experiments were conducted to assess the capability of the proposed approach in identifying reduced order models under biaxial and triaxial loading conditions. The performance of the optimal reduced order models are compared to the direct numerical simulations based on the computational homogenization method, which constitutes the best solution that can be obtained by the reduced order models, since they are derived based on computational homogenization.

Numerical verification analyses are conducted by considering a unidirectional reinforced matrix microstructure with geometry, the discretization and the loading conditions are shown in Fig. 2.4. The finite element discretization of the unit cell consists of 351 tetrahedra. The matrix and the reinforcements are discretized using 251 and 98 elements, respectively. A unit cube discretized using a single hexahedral finite element constitutes the macroscale domain. The volume fraction of the reinforcement within the unit cell is 40%.

The numerical verifications consist of the identification of the optimal reduced order model partitioning based on a small number of load cases, which is then followed by

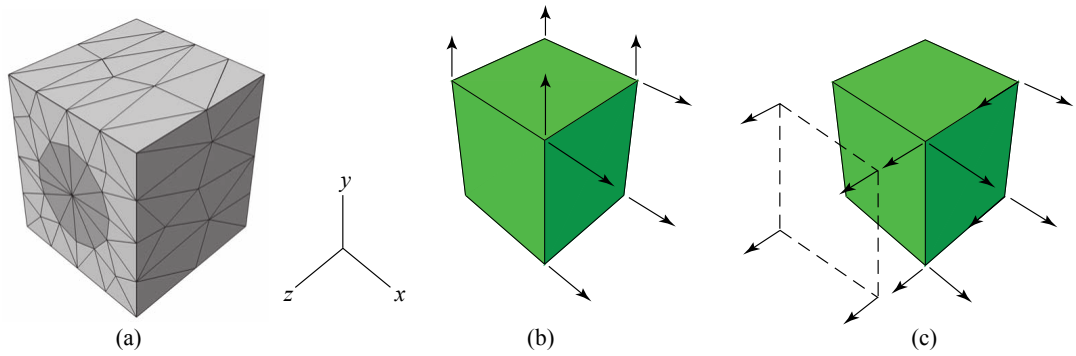

Figure 2.4: Geometry and discretization of the numerical example. (a) Microstructure; (b) Macrostructure subjected to biaxial tensile loading; (c) Macrostructure subjected to combined biaxial tensile and shear loading.

parameter scaling and assessment of model performance using a wider range of loading conditions. A reduced order model is named based on the load cases employed in the identification step and the model order, n. T_i and S_{ij} denote uniaxial loading along the i-direction ($i = x, y, z$) and shear loading along the ij-direction, respectively. For instance, model T_x-S_{xz}-4 indicates a model of order 4 ($n = 4$) identified based on uniaxial tensile loading in the x-direction and shear loading in xz-direction (i.e., $n_{load} = 2$).

The parameters associated with the genetic algorithm are identical for all numerical experiments considered. The population size, n_{pop}, is taken to be 100. The predefined tolerance for convergence due to the fitness of the best individual is taken to be 100. The number of stall generations is set to 40 and the tolerance for convergence due to stall is set to 1e-6. The mutation ratio, which is the portion of the population that is mutated at each generation, is set to 0.01. The identification analyses are conducted using eight parallel compute nodes (p = 8).

2.5.1 Biaxial tensile loading

The performance of the reduced order models are assessed under the condition of biaxial loading perpendicular to the direction of the reinforcement. The elastic modulus and Poisson's ratio for the reinforcements are $E^{(f)} = 200$ GPa and $\nu^{(f)} = 0.3$, and for the matrix

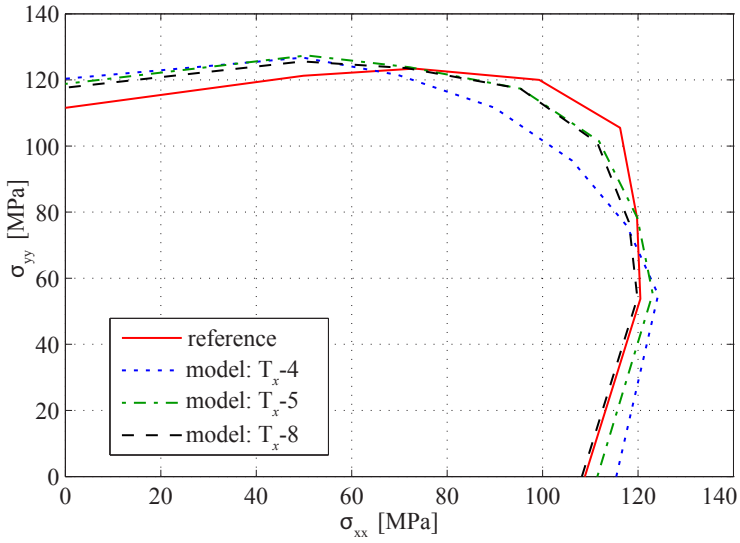

Figure 2.5: Failure envelopes for models T_x-4, T_x-5 and T_x-8 when subjected to tensile loading in x- and y-directions.

are $E^{(m)} = 6$ GPa and $\nu^{(m)} = 0.3$. The reinforcement is taken to be linear elastic, whereas the matrix is modeled using the continuum damage mechanics model with the material parameters of $a^{(m)} = 32.0$ and $b^{(m)} = 16.3$. Each part within the matrix phase is taken to have the same material parameters. In all configurations considered, the entire reinforcement phase is taken to be a single part.

Figure 2.5 illustrates the accuracy of three reduced order models identified under uniaxial tensile loading in the x-direction. The stress envelopes computed using parameter-scaled models T_x-4, T_x-5 and T_x-8 display a reasonable match with the failure envelope computed using the reference computational homogenization method. The parameter scaling constants for models T_x-4, T_x-5 and T_x-8 are 0.87, 0.93 and 0.93, respectively. The modeling error after parameter scaling are respectively, 7.4%, 5.6% and 5.4% for the three models considered. A slight increase in the accuracy is observed with increasing model order for reduced order models with parameter scaling. The increase in accuracy as a function of model order is more pronounced in unscaled models with modeling errors of 17%, 11% and 9.7% for models T_x-4, T_x-5 and T_x-8, respectively, yet the impact of parameter scaling on the model accuracy is evident.

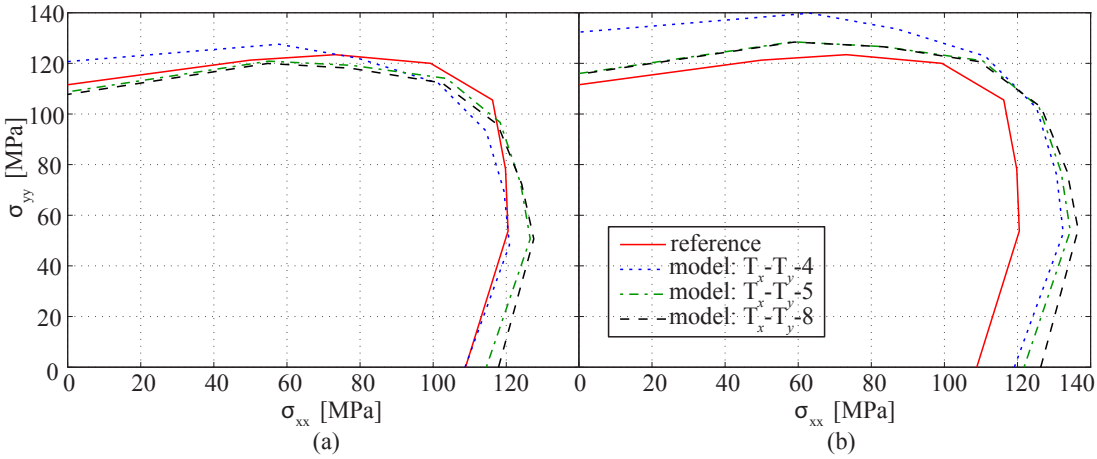

Figure 2.6: Failure envelopes for models T_x-T_y-4, T_x-T_y-5 and T_x-T_y-8 when subjected to tensile loading in x- and y-directions: (a) after parameter scaling; (b) before parameter scaling.

Figure 2.6 shows the failure envelopes of the three additional reduced order models identified under the combined uniaxial tension in the x- and y-directions (i.e., n_{load}=2) compared to the reference simulations after (Fig. 2.6a) and before (Fig. 2.6b) parameter scaling. The model errors prior to parameter scaling are 11.2%, 8.2% and 9.1% for T_x-T_y-4, T_x-T_y-5 and T_x-T_y-8, respectively, whereas the model errors with parameter scaling are respectively, 6.1%, 4.8% and 5.5%. The failure envelopes computed by the unscaled reduced order models clearly show stiff response compared to the computational homogenization model, despite similar shape of the envelope and parameter scaling provides a significant improvement on the accuracy of the models. The errors clearly indicate that the accuracy is a non-monotonic function of the model order, and T_x-T_y-5 marginally outperforms T_x-T_y-8. Higher model orders do not include lower orders as subsets as each part is constrained to contain at least a single finite element. The optimal reduced order model partitions at orders 4, 5, and 8 are shown in Fig. 2.7. The model performance of the reduced order models identified using a single load case is comparable to that with two load cases due to the symmetry of the unit cell with respect to the loading directions. The ideal failure envelope is circular because of the symmetry of the microstructure with respect to the loading considered. The failure envelopes computed using the reference model as well

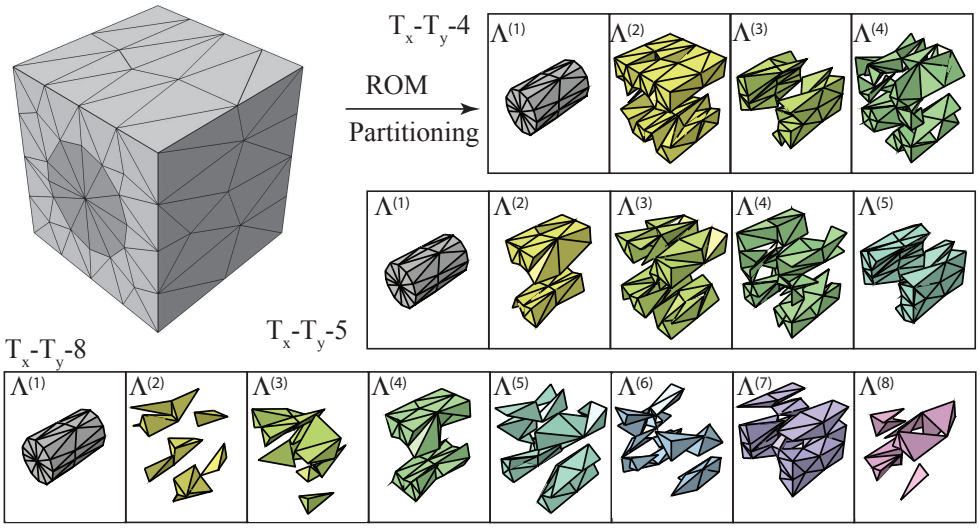

Figure 2.7: Optimal reduced order model partitioning's for models T_x-T_y-4, T_x-T_y-5 and T_x-T_y-8.

as the reduced order models deviate from the circular shapes due to the relatively coarse discretization of the microstructure.

Figure 2.8 illustrates the stress-strain response as computed using the models T_x-T_y-4, T_x-T_y-5 and T_x-T_y-8, and the computational homogenization model when subjected to uniaxial loading (Fig. 2.8a-b) and under the biaxial loading with prescribed displacement ratio of $g_x/g_y = 1.5$ (Fig. 2.8c-d). In addition to accurately capturing the ultimate strength, the reduced order models capture the entire stress-strain response.

2.5.2 Combined biaxial tensile and shear loading

In the current example, a reduced order model for laminated unidirectional reinforced composites is developed. In laminated composites, the plies are typically subjected to a combined state of normal stresses along the reinforcement and transverse directions as well as shear stresses that develop due to the mismatch between neighboring ply orientations. A graphite fiber (IM-7) reinforced epoxy (977) resin is considered. The elastic modulus and Poisson's ratio for the reinforcements are $E^{(f)} = 263$ GPa and $\nu^{(f)} = 0.32$, and for the matrix are $E^{(m)} = 3.55$ GPa and $\nu^{(m)} = 0.35$. Damage is considered in both matrix and

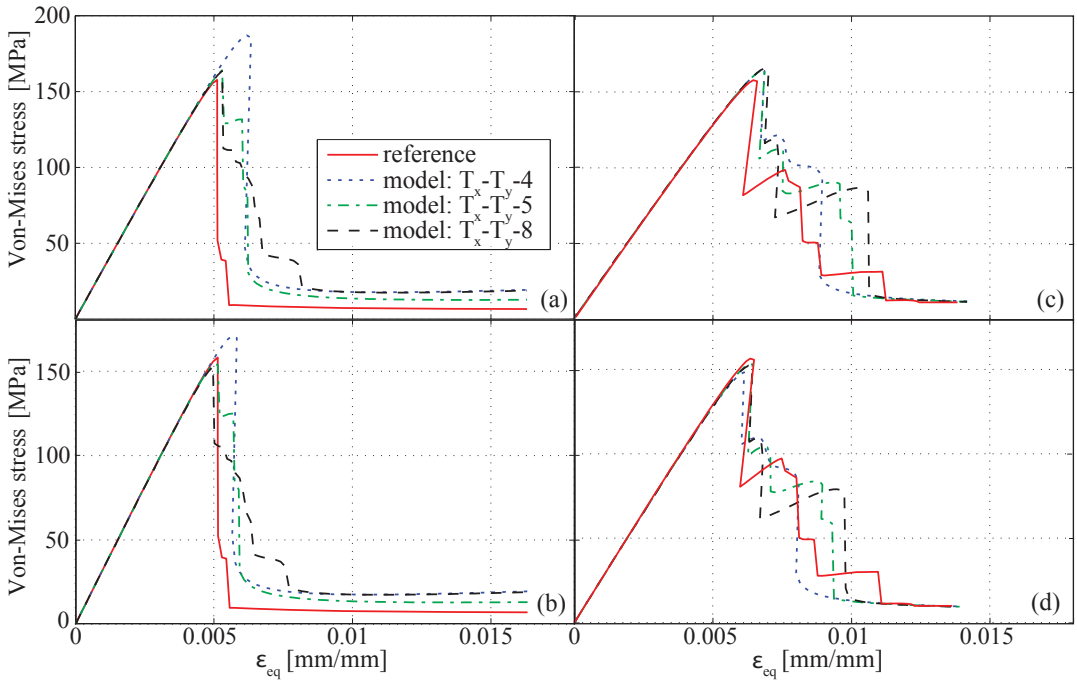

Figure 2.8: Stress-strain curves: (a) unscaled models subjected to unaxial tension in y-direction, (b) parameter scaled models subjected to unaxial tension in y-direction, (c) unscaled models subjected to biaxial loading, and (d) parameter scaled models subjected to biaxial loading.

fiber phases with the material parameters of $a^{(m)} = 0.1$ and $b^{(m)} = 65$ for the matrix phase and $a^{(f)} = 0.1$ and $b^{(f)} = 300$ for the fiber phase.

The reduced order model, T_x-S_{xz}-5, is identified under the uniaxial tensile loading in the transverse direction and shear ($n_{load} = 2$). A single part is assigned to the fiber phase since a sudden fiber failure that predominate the strength in the reinforcement direction is very well captured by a single part. Figure 2.9 shows the two-dimensional failure envelope along the combined transverse normal and shear directions as computed using T_x-S_{xz}-5 and the reference computational homogenization model. The parameter scaling constants for the fiber and matrix parts are 1.0 and 0.69, respectively. The reduced order model provides a good approximation to the reference model. Figure 2.10 shows the three-dimensional failure envelope as computed by the reference (Fig. 2.10a) and the reduced order (Fig. 2.10b) models for combined biaxial tensile and shear loading configurations. The predictions of T_x-S_{xz}-5

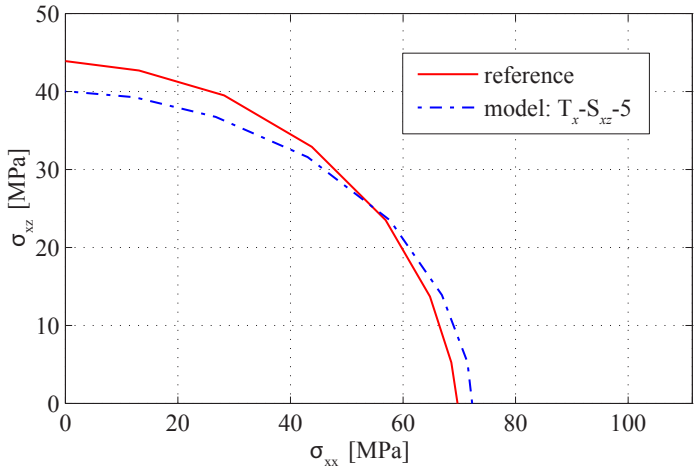

Figure 2.9: Failure envelope for model T_x-S_{xz}-5 when subjected to transverse tensile and shear loading.

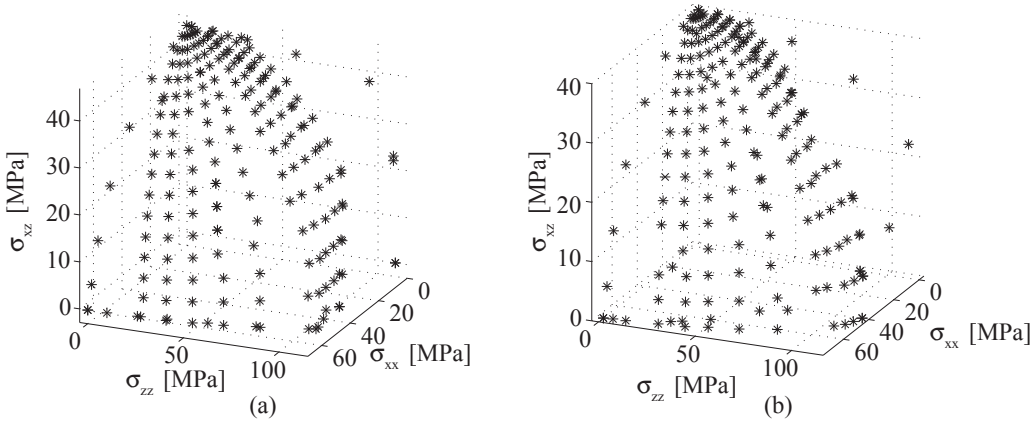

Figure 2.10: Three dimensional failure envelopes when subjected to combined tensile loading in reinforcement and transverse directions, and shear: (a) the reduced order model, T_x-S_{xz}-5; and, (b) the reference model.

for all possible loading scenarios are satisfactory when compared to the reference solution. The predictions of the stress-strain response of the reduced order model are compared to the computational homogenization model in Fig. 2.11. The stress-strain response when the material is subjected to loading in the reinforcement direction is naturally dominated by the fiber behavior (Fig. 2.11a). More complex matrix dominated failure is observed at loading in the transverse (Fig. 2.11b), shear (Fig. 2.11c) and biaxial loading along the reinforcement and transverse directions with applied displacement ratio of $g_x/g_z = 0.75$ (Fig. 2.11d).

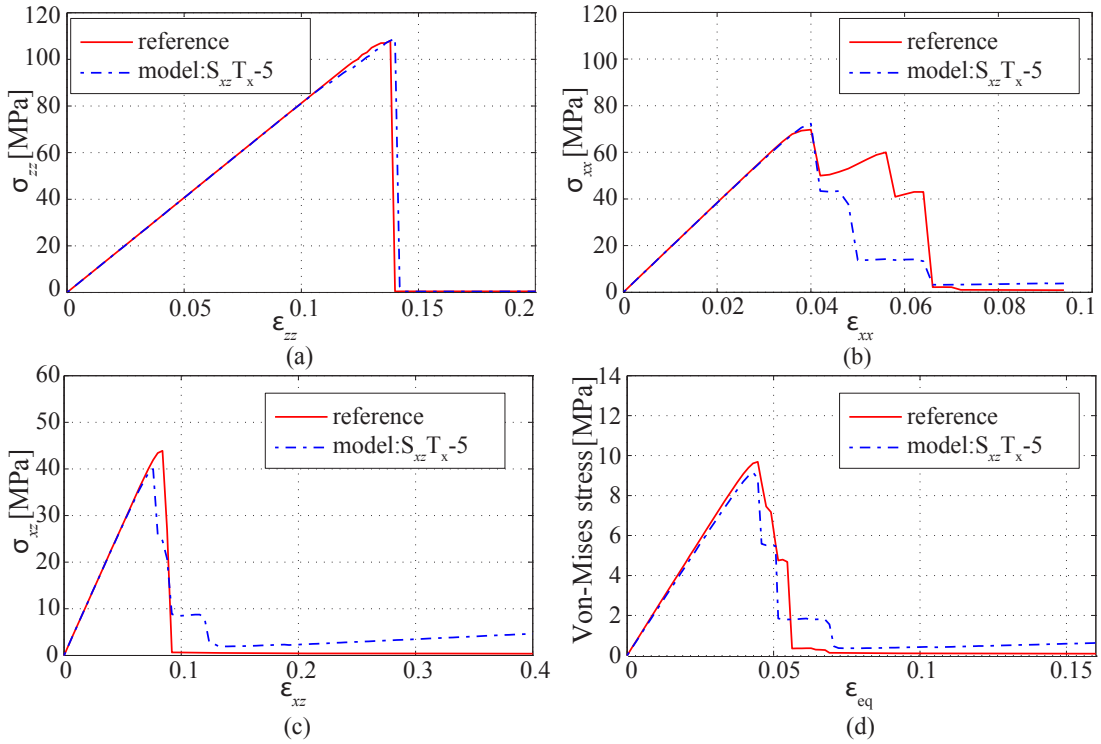

Figure 2.11: Stress-strain curves when subjected to: (a) uniaxial tension in the reinforcement direction; (b) uniaxial tension in the transverse direction; (c) shear, and (d) biaxial tension in the reinforcement and transverse directions.

Chapter 3

REDUCED ORDER HOMOGENIZATION OF HETEROGENEOUS MATERIALS WITH OVERLAPPING FAILURE PATHS

3.1 Introduction

Computational homogenization has emerged as a powerful modeling and simulation tool for structures made of composite and other heterogeneous materials. The computational homogenization method is based on the mathematical homogenization theory and was formalized by Babuska [13], Bensoussan [14], Suquet [15], and Sanchez-Palencia [16]. The computational homogenization method has been used to evaluate the elastic, inelastic, viscous and damage effects [17, 18], geometric nonlinearities [19, 20] and multiphysics response [21, 22]. Recently, the computational homogenization approach is being used to predict the model failure and cracking phenomena in composite materials [23, 24, 25]. One of the main challenges of computational homogenization is the computational complexity involved in solving boundary value problems (BVP) at two (or more) scales. Major progress in reducing the computational cost of the computational homogenization method has been made using the boundary element method [33], the Voronoi cell method [34], the method of cells [35], the fast Fourier transforms [36], the network approximation method [37], the proper orthogonal decomposition [38] and the proper generalized decomposition [39]. To properly characterize the nonlinear response, most reduced order model (ROM) approaches use a small number of functions to span the basis of the microstructural domain as compared to a fully resolved microscale BVP. The accuracy of the ROM depends on the partitioning model order. Hence, choosing the appropriate basis functions to represent the fine scale response is therefore a very critical question.

Eigendeformation-based reduced order homogenization method is an effective approach

that can be applied to problems involving material nonlinearities [1, 2, 3], as well as interface decohesion at the microstructural scale [4, 5]. This approach employs the transformation field analysis (TFA) [6, 7] and evaluates the nonlinear microscale problem using only a small set of unknowns through construction of microstructural influence functions and localization operators that are pre-computed using linear elastic microscale problems. As mentioned before, many ROMs rely on representing the nonlinear response of the full scale microscale BVP using a small number of functions spanning a basis that has dimensions much smaller in comparison. In nonlinear problems, the microstructure loading may change significantly during a loading period due to load redistribution. While the reduced order models are accurate in the load conditions at which they are derived, their performance at full load spectrum is not always accurate and is duly noted [4, 5, 49].

To properly characterize the nonlinear response, the use of a small number of functions spanning the basis of the microstructural domain directly translates to a reduced number of internal state variables to approximate the overall behavior of the ROM. Sparks and Oskay [49] have proposed using a brute force heuristic genetic algorithm (GA) to find the optimal ROM partitioning. The optimal ROM is posed as an nonlinear integer optimization problem (NIOP) provided reasonable results but even with parallel computing, the GA proved to be computationally intractable due to its brute force search for the global minimizer. This can become an issue if the geometry of the microstructure becomes more complex and finer mesh resolutions are used within the microstructure.

The ROM partitioning strategy used in this chapter utilizes the method of failure paths [5]. The potential failure paths are selected as the reduce order model basis. In order to further reduce the computational time, without compromising the accuracy of the results, the potential crack path process zones are allowed to intersect and that the collection of these overlapping parts will characterize the domain of the ROM. Allowing for these overlapping parts further reduces the number of internal state variables in the model as well as the model order, hence computational cost savings. This assumption yields reasonable

results but there is still room for improvement.

During post-processing of the analysis, spurious residual stresses were observed post failure. These observations have been duly noted throughout the literature [4, 12] and this so-called inclusion locking phenomenon has been an issue in need of mitigation. Fish and co-workers propose that the reasoning of this phenomenon is due to the overall macroscopic stress having residual contributions from the elastic deformation of the fiber phase if the matrix phase is exhibiting a perfectly plastic behavior [12]. The notion of these impotent (harmless) eigenstrain terminology has been suggested in the literature by T. Mura, R. Furuhashi [50] and these eigenstrains are either coined as being incompatible or compatible. To alleviate this overly stiff phenomenon and to improve the accuracy of the ROM, modified 'zero mode' impotent eigenstrains are incorporated into the constitutive framework to help predict the overall material response. The consideration of these modified 'zero mode' impotent eigenstrains are a novel contribution because multiple sets of coefficient tensors are computed *a-prior* to the macroscale analysis. Thus, they are computed one time and stored away for later use during the macroscale stress update of the ROM analysis, as opposed to recomputing the coefficient tensors which is computationally prohibitive.

In this chapter, a non-local multiscale model for failure analysis of heterogeneous materials using the eigendeformation-based reduced order homogenization method is presented. A two-scale asymptotic expansion is used to decompose the problem into a macro and microscale BVP and a variant of the transformation field analysis is used to reduce the computational cost of direct homogenization. The ROM partitioning strategy utilizes the method of failure paths, in which the representative volume element is subjected to various loading modes until damage is induced on the microstructure, yielding potential non-local failure crack paths. These potential failure crack paths have a failure process zone on the order of the non-local characteristic length and a crack can occur in this zone. In order to further reduce the computational time, these potential crack path process zones are allowed to intersect and they form overlapping parts which will characterize the domain of the ROM

and reduce the number of internal state variables in the model as well as the model order. To improve the accuracy of the ROM, a modified 'zero mode' impotent eigenstrains is incorporated into the constitutive framework to help predict the overall material response and alleviate these spurious residuals post failure.

The proposed eigendeformation-based reduced order homogenization methodology addresses the following shortcomings (1) how to identify the model order of the reduced basis for a microstructure using the method of failure paths [5] in nonlocal continuum damage model; (2) attention is given to account for the effect of overlapping failure paths in the microscopic domain when using combinatorics to identify the partition for the reduced order model. Lastly, (3) the reduced order model does not capture the post-failure response of the representative volume element accurately. To address this issue of inclusion locking, a new set of coefficient tensors which exhibit a near "zero" mode is generated in the reduced order coarse-scale stress computation.

The remainder of this chapter is as follows: The problem statement is defined on a composite domain in Section 3.2. The macroscale and microscale boundary value problems in the context of the computational homogenization method are described in Section 3.3. In Section 3.4, eigendeformation-based reduced order homogenization is employed in the formulation to solve for the microscale response, the idea of overlapping failure paths is presented, and a modified 'zero mode' impotent eigenstrain formulation as noted in [12] is introduced to alleviate post failure residual stresses. In Section 3.5, the continuum damage mechanics model is defined and a new nonlocal equivalent strain driver is utilized. The computational aspects of the reduced order model development strategy is presented in Section 3.6. Numerical verification examples of the representative volume element (RVE) are large scale beam bending examples are discussed in Section 3.7.

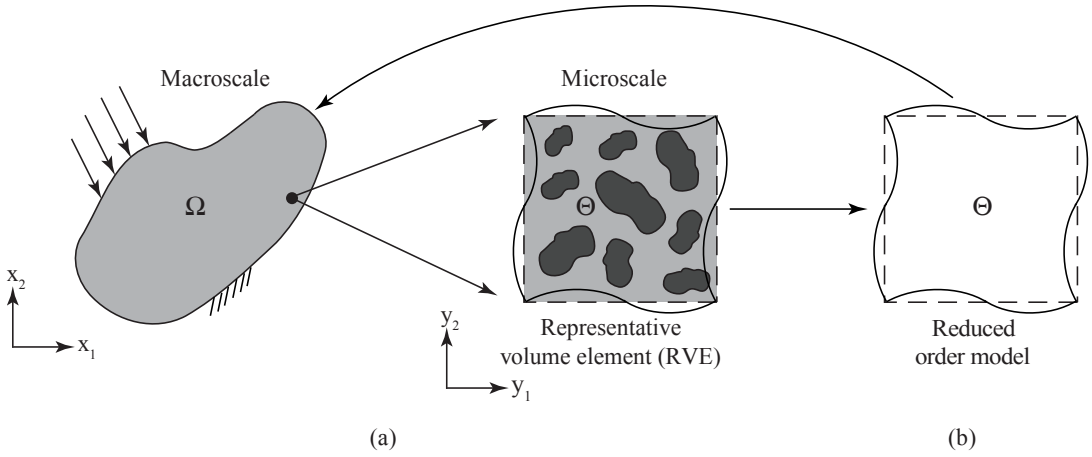

Figure 3.1: Macro- and microscopic structures.

3.2 Problem Statement

A heterogeneous structure with macroscopic domain, Ω, is formed by repetition of the locally periodic microstructure as illustrated in Fig. 3.1. The periodic microstructure consists of $c \geq 2$ constituent phases (as shown in Fig. 3.1a), and the local domain is denoted as Θ. The response fields (e.g., strain, displacement, stress) are functions of the macroscopic and microscopic coordinate systems, and these domains are parameterized by the position vectors, $\mathbf{x}$ and $\mathbf{y}$, respectively. These response fields are assumed to be periodic about the representative volume element. The ratio between the size of the macroscopic and microscopic domains are related by a small positive size scale ratio, ζ, (i.e., $0 < \zeta \ll 1$), such that $\mathbf{y} = \mathbf{x}/\zeta$.

Assuming small deformation theory applies, the governing equations on a macroscopic composite domain, Ω, are outlined as:

$$\sigma^{\zeta}_{ij,j}(\mathbf{x},t) + b^{\zeta}_{i}(\mathbf{x},t) = \rho^{\zeta}\ddot{u}^{\zeta}_{i}(\mathbf{x},t) \qquad \mathbf{x} \in \Omega \tag{3.1}$$

$$\sigma^{\zeta}_{ij}(\mathbf{x},t) = L^{\zeta}_{ijkl}(\mathbf{x})(\varepsilon^{\zeta}_{kl}(\mathbf{x},t) - \mu^{\zeta}_{kl}(\mathbf{x},t)) \equiv [1 - \dot{\omega}^{\zeta}(\mathbf{x},t)]L^{\zeta}_{ijkl}(\mathbf{x})\varepsilon^{\zeta}_{kl}(\mathbf{x},t) \qquad \mathbf{x},\mu \in \Omega \tag{3.2}$$

$$\varepsilon^{\zeta}_{ij}(\mathbf{x},t) = u^{\zeta}_{(i,j)}(\mathbf{x},t) \equiv \frac{1}{2}(u^{\zeta}_{i,x_j} + u^{\zeta}_{j,x_i}) \qquad \mathbf{x} \in \Omega \tag{3.3}$$

$$\dot{\omega}^{\zeta} = \hat{\omega}^{\zeta}(\sigma_{ij}^{\zeta}, \varepsilon_{ij}^{\zeta}, s_{ij}^{\zeta}) \qquad \omega \in \Omega \tag{3.4}$$

where $u_i^{\zeta}(\mathbf{x})$ denotes displacement, $\sigma_{ij}^{\zeta}(\mathbf{x})$ denotes the Cauchy stress and $\varepsilon_{kl}^{\zeta}(\mathbf{x})$ the total strain that can be additively decomposed into the elastic strain and the inelastic strain $\mu_{ij}^{\zeta}(\mathbf{x})$. A subscript comma denotes differentiation, parentheses in the subscript denotes a symmetric differentiation (i.e., u_{i,x_j}^{ζ}). $b_i^{\zeta}(\mathbf{x})$ is the body forces, L_{ijkl}^{ζ} the tensor of elastic moduli. $\omega \in [0,1)$ is the damage variable with $\omega = 0$ and $\omega \to 1$ indicating the states of no damage and complete loss of load carrying capacity. The evolution of the damage variable is explicitly defined in Section 3.5.

The initial and boundary conditions are assumed to be function of the macroscopic coordinates:

$$u_i^{\zeta}(\mathbf{x},t) = \hat{u}_i(\mathbf{x}) \qquad \mathbf{x} \in \Omega, \quad t = 0 \tag{3.5}$$

$$\dot{u}_i^{\zeta}(\mathbf{x},t) = \hat{v}_i(\mathbf{x}) \qquad \mathbf{x} \in \Omega, \quad t = 0 \tag{3.6}$$

$$u_i^{\zeta}(\mathbf{x},t) = \bar{u}_i(\mathbf{x},t) \qquad \mathbf{x} \in \partial\Omega^u, \quad t \in [0,t_0] \tag{3.7}$$

$$\sigma_{ij}^{\zeta}(\mathbf{x},t)n_j = \bar{t}_i(\mathbf{x},t) \qquad \mathbf{x} \in \partial\Omega^t, \quad t \in [0,t_0] \tag{3.8}$$

in which $\bar{u}_i(\mathbf{x})$ and $\bar{t}_i(\mathbf{x})$ are the prescribed displacement and tractions on the boundaries $\partial\Omega^u$ and $\partial\Omega^t$, where $\partial\Omega^u \cup \partial\Omega^t = \partial\Omega$ and $\partial\Omega^u \cap \partial\Omega^t = \emptyset$. n_j is the unit normal to $\partial\Omega^t$.

A general form of the response field, f is expressed in terms:

$$f^{\zeta}(\mathbf{x}) = f(\mathbf{x}, \mathbf{y}(\mathbf{x})), \tag{3.9}$$

where, superscript ζ indicates the oscillatory behavior of the response field due to the local microstructural heterogeneities. It is important to note that Eq. 3.9 is a function of both the macroscopic and microscopic coordinate systems. Utilizing the chain rule, the macroscopic

spatial derivative, has the form:

$$f^{\zeta}_{,x_i}(\mathbf{x}) = f_{,x_i}(\mathbf{x},\mathbf{y}) + \frac{1}{\zeta} f_{,y_i}(\mathbf{x},\mathbf{y}), \tag{3.10}$$

where, $i = 1,2,...,n_{sd}$ and a comma appearing in the subscript indicates taking the partial derivative with respect to the components. The response fields are assumed to be locally periodic throughout the deformation process and are denoted as:

$$f(\mathbf{x},\mathbf{y})) = f(\mathbf{x},\mathbf{y}+\mathbf{k}\hat{\mathbf{y}})) \tag{3.11}$$

in which, $\hat{\mathbf{y}}$ represents the periods of the micro-structure and $\mathbf{k}$ is a $n_{sd} \times n_{sd}$ diagonal matrix consisting of integer entries.

3.3 Computational Homogenization

The coupled boundary value problems which describes the equivalent homogeneous domain (i.e., the macroscale problem) and representative volume element (i.e., the microscale problem) are formed following the mathematical homogenization theory with multiple spatial scales [14]. The displacement field of the heterogeneous material is decomposed using a two-scale asymptotic expansion:

$$u_i(\mathbf{x},\mathbf{y},t) = \bar{u}_i(\mathbf{x},t) + \zeta u^1_i(\mathbf{x},\mathbf{y},t) \tag{3.12}$$

in which, $\bar{u}_i$ and u^1_i are the macroscopic and microscopic displacement fields, respectively. The first order displacement field is independent of the microscale coordinates. The two-scale decomposition of the displacement field is substituted into the equilibrium governing equation and asymptotically expanding the displacement field yields the macro- and microscale BVP counterparts [4]. The strain and stress fields have the same decomposition

and can be expanded using asymptotics analogously.

3.3.1 Macroscale problem

When the two-scale asymptotic decomposition is substituted into the equilibrium equations, considering the $O(1)$ terms and averaging over the representative volume element (RVE) leads to the homogenized macroscale equilibrium equation defined over the macroscopic domain, $\mathbf{\Omega}$:

$$\bar{\sigma}_{ij,x_j}(\mathbf{x},t) + \bar{b}_i(\mathbf{x},t) = 0 \tag{3.13}$$

in which, $\bar{\sigma}_{ij}$ and $\bar{b}_i$ denote the macroscopic stress tensor and body force, respectively, which are volume-averaged (homogenized) over the domain of the RVE, Θ:

$$\bar{\sigma}_{ij}(\mathbf{x},t) = \left\langle \sigma_{ij} \right\rangle \tag{3.14}$$

$$\bar{b}_i(\mathbf{x},t) = \langle b_i \rangle \tag{3.15}$$

where, the Macaulay brackets indicate averaging over the RVE domain:

$$\langle \cdot \rangle = \frac{1}{|\Theta|} \int_{\Theta} (\cdot) d\mathbf{y} \tag{3.16}$$

$|\Theta|$ is the volume of the RVE. Using the strain decompositions, derived analogously to the displacement and integrating over the domain and combining with the stress field equation as shown in [4]. The stress field is expressed as:

$$\sigma_{ij}(\mathbf{x},\mathbf{y},t) = L_{ijkl}(\mathbf{y}) \left[\bar{\varepsilon}_{kl}(\mathbf{x},t) + u^1_{(k,y_l)}(\mathbf{x},\mathbf{y},t) - \mu_{kl}(\mathbf{x},\mathbf{y},t) \right] \tag{3.17}$$

where, L_{ijkl} is the fourth order tensor of elastic moduli, taken to be symmetric and strongly elliptic. L_{ijkl} varies within the RVE due to material heterogeneity but is taken to be constant in macroscale coordinates. $\bar{\varepsilon}_{ij} = \bar{u}_{(i,x_j)}$ is the macroscopic strain tensor. The boundary

conditions of the macroscale problem are defined as:

$$\bar{u}_i(\mathbf{x},t) = g_i(\mathbf{x},t); \quad \mathbf{x} \in \Gamma_u \tag{3.18}$$

$$\bar{\sigma}_{ij}(\mathbf{x},t)\, n_j = t_i(\mathbf{x},t); \quad \mathbf{x} \in \Gamma_t \tag{3.19}$$

in which, g_i is the boundary displacement data prescribed on $\Gamma_u \subset \partial\Omega$; and, t_i is the boundary traction data prescribed on $\Gamma_t \subset \partial\Omega$, such that $\Gamma_u \cap \Gamma_t = \emptyset$ and $\Gamma_u \cup \Gamma_t = \partial\Omega$. The prescribed boundary conditions are taken to vary with respect to the macroscopic scale only and are constant with respect to the microscopic coordinates.

3.3.2 Microscale problem

Substituting the two-scale asymptotic decomposition into the equilibrium equations, considering the $O(\zeta^{-1})$ terms leads to the formulation of the microscale equilibrium equation defined over the RVE domain, Θ:

$$\sigma_{ij,y_j}(\mathbf{x},\mathbf{y},t) = 0 \tag{3.20}$$

Equation 3.20 along with the evolution equations for damage are evaluated for the microscale displacement field, u_i^1, where the macroscopic strain, $\bar{\varepsilon}_{ij}$ acts as the loading function for the microscale problem. The boundary condition of the microscale problem is taken to be periodic. For a rectangular (or cuboidal) shaped RVE domain, the boundary is split into n_{sd} subdomains denoted by Γ_ξ, where $n_{\text{sd}} = 2$ or 3 is the number of spatial dimensions. The RVE boundary consists of multiple pairs of parallel sides (or faces) within each boundary subdomain. The periodic boundary conditions are expressed as:

$$u_i^1(\mathbf{y},t) = u_i^1\left(\mathbf{y} - l_\zeta \mathbf{n}_\xi, t\right); \quad \mathbf{y} \in \Gamma_\xi; \quad \xi = 1,\ldots,n_{\text{sd}} \tag{3.21}$$

in which, $\mathbf{n}_\xi$ is the unit outward normal on Γ_ξ, and l_ξ is the length of the RVE along $\mathbf{n}_\xi$. The nonlinear microscale BVP is solved to evaluate the microscale displacement field, $u^1(\mathbf{x},\mathbf{y},t)$ by enforcing these periodic boundary conditions. In order to restrict rigid body motion, zero microscale displacement is imposed at the vertices of the RVE domain.

3.4 Reduced Order Homogenization

When solving linear problems, the linearity of the microscale displacement field with respect to the macroscopic strains is exploited to pose the microscale problem as the product of the third order influence function, H_{ikl} (i.e., $u_i^1(\mathbf{x},\mathbf{y}) = H_{ikl}(\mathbf{y})\,\bar{\varepsilon}_{kl}(\mathbf{x})$), and scaling the term by the macroscale strain field. The macroscale stress is then a function of H_{ikl}. H_{ikl} is obtained by substituting the above expression into the microscale BVP and then solving the microscale problem when the microscale problem is free of damage (i.e, $\omega = 0$). The influence function is computed numerically by solving the elastic influence function problem and then employed in the evaluation of the macroscale problem. When evaluating these nonlinear problems, the microscale displacement field is typically a nonlinear and history-dependent function of the macroscale strain field. Therefore, a separate microscale problem is assigned to each integration point of a macroscale problem and evaluated for every load increment and iteration of a macroscale analysis. Hence, there is a strong coupling between the macroscale and microscale BVP and the computational burden in this approach is tremendous in case of large structural simulations or when the microstructure is complex. The eigendeformation-based reduced order homogenization approach [4, 5] was employed to develop a reduced order model for efficiently solving for the microscale response. The microscopic displacement field is expressed as:

$$u_i^1(\mathbf{x},\mathbf{y},t) = H_{ikl}(\mathbf{y})\,\bar{\varepsilon}_{kl}(\mathbf{x},t) + \int_\Theta h_{ikl}(\mathbf{y},\hat{\mathbf{y}})\,\mu_{kl}(\mathbf{x},\hat{\mathbf{y}},t)\,d\hat{\mathbf{y}} \tag{3.22}$$

The inelastic influence function, h_{ikl}, is a type of numerical Green's function and consists of the particular solutions of the RVE and is approximated as numerical solutions on the linear elastic RVE problems. The numerical evaluation of the elastic and damage influence functions are provided in [4] and skipped herein for brevity.

The computational complexity of solving the RVE problem is reduced by the discretization of the eigendeformation fields, using the following expression:

$$\mu_{ij}(\mathbf{x},\mathbf{y},t) = \sum_{\alpha=1}^{n} N^{(\alpha)}(\mathbf{y})\,\mu_{ij}^{(\alpha)}(\mathbf{x},t) \tag{3.23}$$

where, $N^{(\alpha)}$ is the mesomechanical shape function; n is the order of discretization (also referred to as the model order), and $\mu_{ij}^{(\alpha)}$ are the microscopically nonlocal inelastic strain coefficients expressed as:

$$\mu_{ij}^{(\alpha)}(\mathbf{x},t) = \int_{\Theta} \varphi^{(\alpha)}(\mathbf{y})\,\mu_{ij}(\mathbf{x},\mathbf{y},t)\,d\mathbf{y} \tag{3.24}$$

in which, $\varphi^{(\alpha)}$ are mesomechanical weight functions. The mesomechanical shape functions differ from the standard finite element shape functions in the sense that they are coarser and requires only C^{-1} continuity. Analogously, the phase damage $\omega^{(\alpha)}$ has a similar expression as Eq. 3.24. The strain field of the heterogeneous material is decomposed using a two-scale asymptotic expansion and consist of a macroscopic and microscopic contribution. Employing the discretized inelastic strain field shape function and integrating over the domain of the RVE, a kinematic relationship between the nonlocal inelastic strain coefficients and nonlocal total strain coefficient is obtained:

$$\varepsilon_{ij}^{(\alpha)}(\mathbf{x},t) = A_{ijkl}^{(\alpha)}\bar{\varepsilon}(\mathbf{x},t) + \sum_{\beta=1}^{n} P_{ijkl}^{(\alpha\beta)}\mu_{kl}^{(\beta)}(\mathbf{x},t) \tag{3.25}$$

where, $\varepsilon_{ij}^{(\beta)}$ is defined analogous to Eq. 3.24, and:

$$A_{ijkl}^{(\alpha)} = I_{ijkl} + \int_{\Theta} \varphi^{(\alpha)}(\mathbf{y})\, G_{ijkl}(\mathbf{y})\, d\mathbf{y} \tag{3.26}$$

$$P_{ijkl}^{(\alpha)} = \int_{\Theta^{(\alpha)}} g_{ijkl}(\mathbf{y},\hat{\mathbf{y}}) N^{(\alpha)}(\mathbf{y}) d\hat{\mathbf{y}} \tag{3.27}$$

$$P_{ijkl}^{(\alpha\beta)} = \int_{\Theta}\int_{\Theta} \varphi^{(\alpha)}(\mathbf{y})\, g_{ijkl}(\mathbf{y},\hat{\mathbf{y}})\, N^{(\beta)}(\hat{\mathbf{y}})\, d\hat{\mathbf{y}} d\mathbf{y} \tag{3.28}$$

$$M_{ijkl}^{(\alpha)} = \frac{1}{\left|\Theta^{(\alpha)}\right|} \int_{\Theta} L_{ijmn}^{(\alpha)}(\mathbf{y}) \left(P_{mnkl}^{(\alpha)}(\mathbf{y}) - I_{mnkl} N^{(\alpha)}(\mathbf{y})\right) d\mathbf{y} \tag{3.29}$$

in which, $G_{ijkl} = H_{(ikl,y_j)}$ and $g_{ijkl} = h_{(ikl,y_j)}$ are elastic and inelastic polarization tensors, respectively; and I_{ijkl} is the fourth order identity tensor. $A_{ijkl}^{(\alpha)}$ is the fourth order elastic strain concentration tensor. $P_{ijkl}^{(\alpha)}$, $P_{ijkl}^{(\alpha\beta)}$ and $M_{ijkl}^{(\alpha)}$ are coefficient tensors providing the microstructural morphology information.

The evolution of the inelastic strains is in terms of the nonlocal variables, has the following form:

$$\dot{\mu}_{ij}^{(\alpha)} = \hat{\mu}_{ij}^{(\alpha)} \left(\varepsilon_{ij}^{(\alpha)}, \mathbf{h}^{(\alpha)}\right) \tag{3.30}$$

where, $\varepsilon_{ij}^{(\alpha)}$ is the nonlocal strain coefficient and $\mathbf{h}^{(\alpha)}$ denotes additional internal state variables defining the evolution of the inelastic process. Analogously, Eq. 3.30 is defined similarly as Eq. 3.4. Equation 3.30 along with Eq. 3.25 are evaluated to obtain $\mu_{ij}^{(\alpha)}$ for a prescribed macroscopic strain state. The computed inelastic strain field satisfies the microscale equilibrium *a-priori* via the influence functions. The evaluation of $\mu_{ij}^{(\alpha)}$ therefore provides an approximation to the solution of the microscale problem. The specific form of the evolution equations Eq. 3.30 requires that the nonlocal inelastic strain coefficients describe the inelastic processes at a subdomain occupied by a single constituent phase.

Considering the particular form of the inelastic strain field, combining with Eq. 3.23 and Eq. 3.17, premultiplying the resulting equation by $\varphi^{(\alpha)}$ and integrating over the unit cell yields the nonlocal inelastic strain coefficients expressed in the following algebraic form

$(\forall \alpha = 1,2,\ldots,n)$:

$$\sum_{\beta=1}^{n} \left[\delta_{\alpha\beta} I_{ijkl} - P_{ijkl}^{(\alpha\beta)} \omega^{(\alpha)}(\mathbf{x},t) \right] \mu_{kl}^{(\beta)}(\mathbf{x},t) - \omega^{(\alpha)}(\mathbf{x},t) A_{ijkl}^{(\alpha)} \bar{\varepsilon}_{kl}(\mathbf{x},t) = 0 \tag{3.31}$$

where, $\delta_{\alpha\beta}$ is Kronecker delta. The constitutive relation for the macroscopic problem is obtained by combining the homogenized stress with the decomposition of the phase damage, $\omega(\mathbf{x},\mathbf{y},t)$, which is defined analogous to the inelastic strain field in Eq. 3.23, and utilizing the definitions of the coefficient tensors. The constitutive relation for the macroscopic problem is:

$$\bar{\sigma}_{ij}(\mathbf{x},t) = \bar{L}_{ijkl} \bar{\varepsilon}_{kl}(\mathbf{x},t) + \sum_{\alpha=1}^{n} \bar{M}_{ijkl}^{(\alpha)} \mu_{kl}^{(\alpha)}(\mathbf{x},t) \tag{3.32}$$

3.4.1 Method of failure paths

The accuracy and computational efficiency of the reduced order model is related to the model order (n) as well as the selection of the shape and weight functions of the ROM. As the model order increase for a particular ROM, the computational complexity increases and ultimately results in a larger set of nonlinear equations that must be evaluated.

Let ${}_i\Theta \subset \Theta$ denote the domain of phase i $(1 \leq i \leq c)$ within the RVE. Consider an alternative decomposition of the domain of the RVE into n possibly intersecting subdomains, with $\Theta^{(\alpha)}$ as the α^{th} subdomain (or part) in the partition. A part is taken to be the subdomain of a single phase: $\Theta^{(\alpha)} \subset {}_i\Theta$ and the overlap of multiple phase domains is not allowed. Hence,

$$\Theta \equiv S_0 \cup \bigcup_{\alpha=1}^{n} \Theta^{(\alpha)} \tag{3.33}$$

where, S_0 is the null set. The intersection between two parts is denoted as $\Theta^{(\alpha\beta)} \equiv \Theta^{(\alpha)} \cap \Theta^{(\beta)}$. A material point within the RVE is allowed to lie in all n parts or less but taken to occupy only those parts that are within the corresponding phase, ${}_i\Theta$. The intersection between multiple parts are defined by repetitive Greek superscripts: $\Theta^{(\alpha\beta\nu\ldots)} \equiv \Theta^{(\alpha)} \cap$

$\Theta^{(\beta)} \cap \Theta^{(\nu)} \ldots$. $\Theta_k^{(\alpha)}$ is further defined as the subdomain of $\Theta^{(\alpha)}$ that intersect precisely $k-1$, other parts $\Theta^{(\beta)}$. Thus, $\Theta_1^{(\alpha)}$ indicates the region exclusively bounded by $\Theta^{(\alpha)}$. Let's suppose, S_k are the subdomains that are in exactly k of the $\Theta^{(\alpha)}$'s. Thus, S_k is *exactly* k intersections of the subdomain, where, $k = 1, 2, \ldots, n$. Hence, $\Theta_k^{(\alpha)} \equiv \Theta^{(\alpha)} \cap S_k$ and $\Theta_k^{(\alpha\beta)} \equiv \Theta^{(\alpha)} \cap \Theta^{(\beta)} \cap S_k$. The definition can be generalized as:

$$\Theta_k^{(\alpha\beta\nu\cdots)} \equiv \Theta^{(\alpha)} \cap \Theta^{(\beta)} \cap \Theta^{(\nu)} \cap \cdots \cap S_k. \tag{3.34}$$

Below is a pictorial illustration of the overlapping subdomains in Θ, which consist of S_k, with *exactly* k intersections. The $\Theta_k^{(\alpha)}$'s are the subdomains of the phase part.

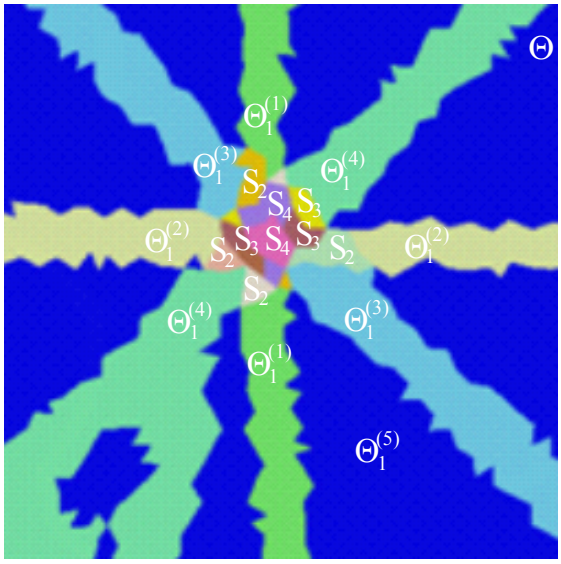

Figure 3.2: Intersections of *exactly* k in the subdomain with the collection of $\Theta^{(\alpha)}$ parts.

The phase shape functions $N^{(\alpha)}$ are assumed to satisfy the partition of unity property:

$$\sum_{\alpha=1}^{n} N^{(\alpha)}(\mathbf{y}) = 1; \;\; \mathbf{y} \in \Theta \tag{3.35}$$

and the phase weight functions, $\varphi^{(\alpha)}$ satisfy positivity:

$$\varphi^{(\alpha)}(\mathbf{y}) \geq 0 \tag{3.36}$$

and normalization condition.

$$\int_{\Theta} \varphi^{(\alpha)}(\mathbf{y}) d\mathbf{y} = 1 \tag{3.37}$$

The various choices of weight and shape functions and the significance of using non-orthogonal basis sets in comparison to using an orthogonal basis are explained below. By allowing the parts within the failure paths to overlap, the number of equations that have to be solved in the system are effectively reduced. A basis which is formed by non-orthogonal functions is defined as:

$$S_{ij} = \langle b_i | b_j \rangle = \int b_i^* b_j dv \tag{3.38}$$

where S_{ij} constitutes the overlap matrix, or the quantities are known as overlap integrals and they are assumed to have a basis of n functions b_i. If a particular special case of an orthogonal basis set is considered, then the overlap matrix becomes the identity matrix, $S_{ij} = \delta_{ij}$. With the appropriate choice of orthogonal shape functions, it is a trivial task to show that the shape and weight functions imply orthonormality.

$$\int_{\Theta} \varphi^{(\alpha)}(\mathbf{y}) N^{(\beta)}(\mathbf{y}) dy = \delta^K_{\alpha\beta} \tag{3.39}$$

in which $\delta^K_{\alpha\beta}$ is the Kronecker delta. If a non-orthogonal basis is considered, then S_{ij} is over overall matrix. Hence,

$$S_{\alpha\beta} = \left\langle N^{(\alpha)} | N^{(\beta)} \right\rangle = \int_{\Theta} N^{(\alpha)} * N^{(\beta)} d\mathbf{y} \tag{3.40}$$

The shape functions for the reduced order model, $N^{(\alpha)}$, are chosen as:

$$N^{(\alpha)}(\mathbf{y}) = \begin{cases} 1 & \text{if } \mathbf{y} \in \Theta_k^{(\alpha)} \Big\backslash \bigcup_{\substack{\beta=1 \\ \alpha \neq \beta}}^{n} \Theta_k^{(\alpha\beta)} \\ \dfrac{1}{k} & \text{if } \mathbf{y} \in \Theta_k^{(\alpha)} \cap \Theta_k^{(\beta)} \\ 0 & \text{elsewhere} \end{cases} \tag{3.41}$$

in which, $k = 1, 2, 3, 4, \ldots, n$ and has *exactly* k intersections. The shape functions defined in Eq. 3.41 allow the possibility of intersecting subdomains and do not form an orthogonal basis, instead due to the overlapping nature of the parts, the corresponding shape functions are constructed to form the reduced basis.

Previous investigators [4, 12, 20] have all used an orthogonal basis to form their shape functions, but the overlapping parts can be decomposed by utilizing Gram-Schmidt to construct an orthogonal version of the same basis. The evaluation of the overlap matrix can be posed as a generalized eigenvalue problem and the problem can be decomposed into two equivalent eigenvalue problems. The details of the solution strategy is given in the following lecture notes [51]. Another solution strategy is to evaluate the effect of the stability of the system by calculating the condition numbers.

3.4.2 Identification of parts

The identification of the proper reduced order model for the RVE affects the efficiency and accuracy of the proposed ROMs. As the model order, n increases, the accuracy of the ROM increases at the expense of additional computational effort. There are many approaches which investigates the identification of the proper partitioning strategy. Sparks and Oskay [49] have proposed using a brute force heuristic genetic algorithm (GA) to find the optimal ROM partitioning. The optimal ROM is posed as a nonlinear integer optimization problem (NIOP) provided reasonable results but even with parallel computing, the GA proved to be computationally intractable due to its brute force search for the global

minimizer. This can become an issue if the geometry of the microstructure becomes more complex and finer mesh resolutions are used. Previous investigators [4] have proposed using a dynamic and static partitioning strategy. The dynamic partitioning strategy resembles an h-version adaptive finite element refinement, in which the space is probed based on a pre-defined error metric and once a hot spot has been identified based on the response metric, the model order is increased accordingly. This dynamic partitioning strategy is rigorous and efficiency decreases due to the complication of the adaptive process and there is a significant computational cost. In static partitioning the ROM basis is selected *a-priori* based on your intuition after sufficient probing of the space. In this section, the static partitioning strategy (or method of predetermined failure paths) [5] is used and the RVE domain partition and model order are identified prior to the macroscopic analysis.

A periodic microstructure where the constituent phases, c = 2, consists of matrix material and is reinforced by a fiber is considered. The fiber material is assumed to be isotropic and elastic with no damage accumulation. The matrix phase is allowed to degrade and has damage evolution parameters. The RVE is subjected to various loading modes which are admissible by homogenization theory until damage is induced on the microstructure, yielding potential non-local failure crack paths. The various loading modes are uniform macroscopic strain modes (i.e., uniaxial tensile or shear) which are applied along the boundaries of the microstructure. The potential failure paths are selected as the reduce order model basis using a small number of domain parts (i.e., small model order n). The potential failure crack paths have a failure process zone on the order of the non-local characteristic length and a crack can occur in this zone when these loads are applied. In order to further reduce the computational time, these potential crack path process zones are assumed to intersect and they form overlapping parts which will characterize the domain of the ROM and reduce the number of internal state variables in the model as well as the model order, n.

3.4.3 Modified 'zero mode' impotent eigenstrains

The system for solving the ROM has generally been defined. Once these uniform macroscopic strains are applied to the periodic microstructure, potential failure crack paths are formed. Although, the crack can occur anywhere within this potential failure path, for simplicity sake, the whole path is taken as a failed part and selected as the failure path for that given admissible loading.

During post-processing of the analysis, spurious residual stresses were occurring post failure. These observations have been duly noted throughout the literature [4, 12] and this so-called inclusion locking phenomenon has been an issue in need of mitigation. Fish and co-workers propose that the reasoning of this phenomenon is due to the overall macroscopic stress having residual contributions from the elastic deformation of the fiber phase if the matrix phase is exhibiting a perfectly plastic behavior [12]. The notion of these impotent (harmless) eigenstrain terminology has been suggested in the literature by T. Mura, R. Furuhashi [50] and these eigenstrains are either coined as being incompatible or compatible. To alleviate this overly stiff phenomenon and to improve the accuracy of the ROM, a modified 'zero mode' impotent eigenstrains is incorporated into the constitutive framework to help predict the overall material response. The consideration of these modified 'zero mode' impotent eigenstrains area novel contribution because multiple sets of coefficient tensors are computed *a-prior* to the macroscale analysis. Thus, they are computed one time and stored away for later use during the macroscale stress update of the ROM analysis, as opposed to recomputing the coefficient tensors which is computationally prohibitive.

To demonstrate the effect of residual stress for zero mode eigenstrains, a three part non-overlapping ROM as shown in Fig. 3.3a is considered. Suppose $\omega^{(1)}$=1; $\omega^{(2)}$=$\omega^{(3)}$=0. Using Eq. 3.31:

$$\begin{aligned}\left(I_{ijkl}-P^{(11)}_{ijkl}(\mathbf{y})\omega^{(1)}\right)\mu^{(1)}_{kl}(\mathbf{x},t)-P^{(12)}_{ijkl}(\mathbf{y})\omega^{(1)}\mu^{(2)}_{kl}(\mathbf{x},t)-P^{(13)}_{ijkl}(\mathbf{y})\omega^{(1)}\mu^{(3)}_{kl}(\mathbf{x},t)\\ =\omega^{(1)}A^{(1)}_{ijkl}(\mathbf{y})\bar{\varepsilon}_{kl}(\mathbf{x},t)\end{aligned} \tag{3.42}$$

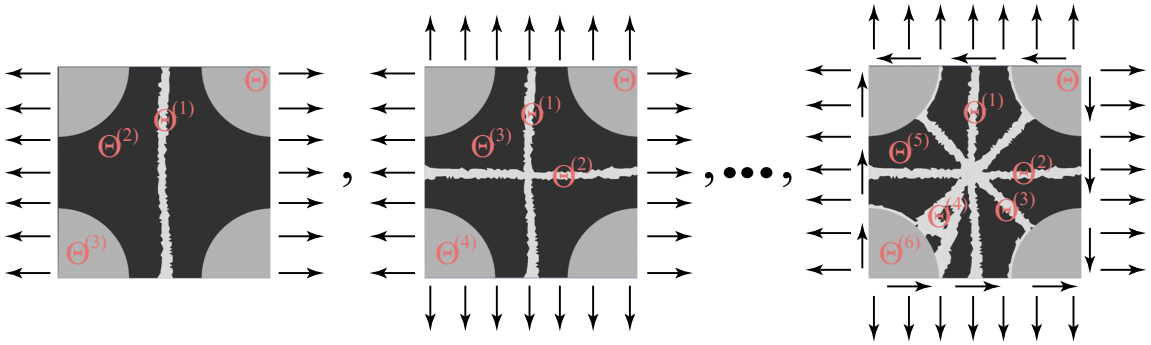

Figure 3.3: New sets of coefficient tensors are generated based on the combination of activated potential failure crack paths, (i.e. zero mode impotent eigenstrains). The dark grey (matrix) and the light grey (fiber) regions retain their original material properties. The white region is the activated potential crack which is idealized as an empty space failure path. (a) Corresponds to $\Theta^{(1)}$ empty space failure path for the given loading; (b) simultaneous $\Theta^{(1)}$ and $\Theta^{(2)}$ potential empty space failure paths which intersect for the given loading; and lastly (c) $\Theta^{(n)}$ simultaneous potential empty space failure paths corresponding to n loading conditions.

$$-P^{(21)}_{ijkl}(\mathbf{y})\omega^{(2)}\mu^{(1)}_{kl}(\mathbf{x},t)+\left(I_{ijkl}-P^{(22)}_{ijkl}(\mathbf{y})\omega^{(2)}\right)\mu^{(2)}_{kl}(\mathbf{x},t)-P^{(23)}_{ijkl}(\mathbf{y})\omega^{(2)}\mu^{(3)}_{kl}(\mathbf{x},t) = \omega^{(2)}A^{(2}_{ijkl}(\mathbf{y})\bar{\varepsilon}_{kl}(\mathbf{x},t) \tag{3.43}$$

$$-P^{(31)}_{ijkl}(\mathbf{y})\omega^{(3)}\mu^{(1)}_{kl}(\mathbf{x},t)-P^{(32)}_{ijkl}(\mathbf{y})\omega^{(3)}\mu^{(2)}_{kl}(\mathbf{x},t)+\left(I_{ijkl}-P^{(33)}_{ijkl}(\mathbf{y})\omega^{(3)}\right)\mu^{(3)}_{kl}(\mathbf{x},t) = \omega^{(3)}A^{(3)}_{ijkl}(\mathbf{y})\bar{\varepsilon}_{kl}(\mathbf{x},t) \tag{3.44}$$

Applying the above damage state conditions to the equations above simplifies to:

$$(I_{ijkl}-P^{(11)}_{ijkl}(\mathbf{y})\omega^{(1)})\mu^{(1)}_{kl}(\mathbf{x},t) = A^{(1)}_{ijkl}(\mathbf{y})\bar{\varepsilon}_{kl}(\mathbf{x},t) \tag{3.45}$$

Thus,

$$\mu^{(1)}_{kl}(\mathbf{x},t) = \left(I_{ijkl}-P^{(11)}_{ijkl}(\mathbf{y})\right)^{-1}A^{(1)}_{ijkl}(\mathbf{y})\bar{\varepsilon}_{kl}(\mathbf{x},t) \tag{3.46}$$

It is therefore a trivial task to see that $\mu^{(2)}_{kl}(\mathbf{x},t)=\mu^{(3)}_{kl}(\mathbf{x},t)=0$.

Substituting Eq. 3.45 into Eq. 3.31:

$$\bar{\sigma}_{ij}(\mathbf{x},t) = \bar{L}_{ijkl}\bar{\varepsilon}_{kl}(\mathbf{x},t) + \bar{M}^{(1)}_{ijkl}\left(I_{ijkl} - P^{(11)}_{ijkl}(\mathbf{y})\right)^{-1} A^{(1)}_{ijkl}(\mathbf{y})\bar{\varepsilon}_{kl}(\mathbf{x},t) \tag{3.47}$$

Note that:

$$N^{(\alpha)}(\mathbf{y}) = \begin{cases} 1 \text{ if } \mathbf{y} \in \Theta^{(\alpha)} \\ 0 \text{ elsewhere} \end{cases} \tag{3.48}$$

$$\varphi^{(\alpha)}(\mathbf{y}) = \frac{1}{\left|\Theta^{(\alpha)}\right|} N^{(\alpha)}(\mathbf{y}) \tag{3.49}$$

where,

$$A^{(1)}_{ijkl} = I_{ijkl} + \frac{1}{\left|\Theta^{(1)}\right|}\int_{\Theta^{(1)}} G_{ijkl}(\mathbf{y})\, d\mathbf{y} \tag{3.50}$$

$$P^{(1)}_{ijkl} = \frac{1}{\left|\Theta^{(1)}\right|}\int_{\Theta^{(1)}} g_{ijkl}(\mathbf{y},\hat{\mathbf{y}}) d\hat{\mathbf{y}} \tag{3.51}$$

$$P^{(11)}_{ijkl} = \frac{1}{\left|\Theta^{(1)}\right|}\int_{\Theta^{(1)}}\int_{\Theta^{(1)}} g_{ijkl}(\mathbf{y},\hat{\mathbf{y}})\, d\hat{\mathbf{y}} d\mathbf{y} \tag{3.52}$$

$$\begin{aligned} M^{(1)}_{ijkl} = \frac{L^{(1)}_{ijmn}(\mathbf{y})}{\left|\Theta^{(1)}\right|}\Big[\Big(\int_{\Theta^{(1)}}\int_{\Theta^{(1)}} g_{mnkl}(\mathbf{y},\hat{\mathbf{y}})\, d\hat{\mathbf{y}} d\mathbf{y} - I_{mnkl}\Big) + \\ \Big(\int_{\Theta^{(1)}}\int_{\Theta^{(1)}} g_{mnkl}(\mathbf{y},\hat{\mathbf{y}})\, d\hat{\mathbf{y}} d\mathbf{y} - I_{mnkl}\Big) + \Big(\int_{\Theta^{(1)}}\int_{\Theta^{(1)}} g_{mnkl}(\mathbf{y},\hat{\mathbf{y}})\, d\hat{\mathbf{y}} d\mathbf{y} - I_{mnkl}\Big)\Big] \end{aligned} \tag{3.53}$$

Simplifying the above expression for $M^{(1)}_{ijkl}$ yields:

$$M^{(1)}_{ijkl} = c^{(1)} L^{(1)}_{ijkl}(\mathbf{y})\left(P^{(11)}_{ijkl}(\mathbf{y}) - I_{ijkl}\right) + c^{(1)} L^{(1)}_{ijkl}(\mathbf{y}) P^{(12)}_{ijkl}(\mathbf{y}) + c^{(1)} L^{(1)}_{ijkl}(\mathbf{y}) P^{(13)}_{ijkl}(\mathbf{y}) \tag{3.54}$$

Hence, the final expression for the homogenized stress is:

$$\begin{aligned} \bar{\sigma}_{ij}(\mathbf{x},t) = \bar{L}_{ijkl}\bar{\varepsilon}_{kl}(\mathbf{x},t) + \Big[c^{(1)} L^{(1)}_{ijkl}(\mathbf{y})\left(P^{(11)}_{ijkl}(\mathbf{y}) - I_{ijkl}\right) + \\ c^{(1)} L^{(1)}_{ijkl}(\mathbf{y}) P^{(12)}_{ijkl}(\mathbf{y}) + c^{(1)} L^{(1)}_{ijkl}(\mathbf{y}) P^{(13)}_{ijkl}(\mathbf{y})\Big]\left(I_{ijkl} - P^{(11)}_{ijkl}(\mathbf{y})\right)^{-1} A^{(1)}_{ijkl}(\mathbf{y})\bar{\varepsilon}_{kl}(\mathbf{x},t) \end{aligned} \tag{3.55}$$

Under the applied loading along the horizontal (1-direction), the overall stress along the same direction has to vanish due to complete separation within the microstructure (i.e., a potential failure path has formed). The computation is generally nonzero, as described in [12, 50]. In the present chapter, the following idea has been implemented. Consider at the point of failure, the tensor of elastic moduli associated with failure path is set to vanish (i.e. $L^{(1)}_{ijkl}(\mathbf{y}) = 0$). The second part of the RHS of Eq. 3.55 consequently vanishes. As illustrated in Fig. 3.3a, it is clear that the components of the homogenized tensor along the 1-direction also vanish, leading to vanishing stress along the direction perpendicular to the direction of the failure path. This simple example was to demonstration the effect of residual stress for zero mode eigenstrains.

Now that a simple example has shown the effect of the residual stress, the details of solving for the original coefficient tensors and generating these multiple sets of coefficient tensors corresponding to these zero mode eigenstrains are provided. A set of coefficient tensors are generated, *a-priori* to the macroscale analysis, which represent the different nonoverlapping and overlapping parts described in Eq. 3.34. When determining the original set of coefficient tensors, the tensor of elastic moduli is utilized. $L^{(\alpha)}_{ijkl}$ is defined as the tensor of elastic moduli of the constituent phase occupying $\Theta^{(\alpha)}$, this $L^{(\alpha)}_{ijkl}$ is taken to be constant throughout the $\Theta^{(\alpha)}$. Utilizing this same $L^{(\alpha)}_{ijkl}$ throughout the $\Theta^{(\alpha)}$ will contribute to the inclusion locking since the rest of the transformation influence functions are a consequence of the elastic boundary value problems, as shown above in the simple three part non-overlapping example.

To alleviate this overly stiff phenomenon, the periodic microstructure described above in Fig. 3.2 is considered and multiple sets of new coefficient tensors are generated. One set of coefficient tensors as described previously are selected, then a series of zero eigenmode coefficient tensors are generated. A new tensor of elastic moduli, $\hat{L}^{(\alpha)}_{ijkl}$ is defined, which is related to phase damage.

Consider the damage in a failure path which is now an empty space. This empty space

can be idealized as a crack and the corresponding $L^{(\alpha)}_{ijkl}$ is now defined by this new $\hat{L}^{(\alpha)}_{ijkl}$. It is shown in Fig. 3.3a, that the dark and light gray regions bounded by $\Theta^{(2)}$ and $\Theta^{(3)}$, respectively, retain their same material properties. The only difference is the white region bounded by $\Theta^{(1)}$ is now idealized as an empty space, therefore the original $L^{(\alpha)}_{ijkl}$ is reduced by a scaling term ι. Hence, $\hat{L}^{(\alpha)}_{ijkl} = \iota L^{(\alpha)}_{ijkl}$. This is the general procedure to generate the first order coefficient tensors for the analysis based on Fig. 3.3a.

The above idea may be generalized to account for multiple sets of newly generated coefficient tensors (i.e., second order, and higher order) based on the combination of activated potential failure crack paths, and this idea is illustrated in Fig. 3.3b-c. For instance, in Fig. 3.3b, if two potential failure paths have activated at the same time (i.e., $\omega^{(\beta)} = \omega^{(\nu)}$ =1), a series of coefficient tensors corresponding to $[\Theta^{(12)}, \Theta^{(13)}, \Theta^{(14)}, \Theta^{(23)}, \Theta^{(24)}, \Theta^{(34)}]$ are generated based on the combination of interacting overlapping failure paths. This same idea can be applied for higher order multiple sets of coefficient tensors, in which all the combinations of potential failure paths are taken into account once activated at the same time for a given loading condition.

To distinguish between the different sets of coefficient tensors, the symbol, $\bar{\varsigma}$ is defined. This corresponds to the collection of all original coefficient tensors, hence, $\bar{\varsigma} = [P^{(\alpha)}_{ijkl}, P^{(\alpha\beta)}_{ijkl}, M^{(\alpha)}_{ijkl}, \cdots]$. Now a new set for the first order zero eigenmode coefficient tensors are defined where, β failure that has degraded. Thus, $\tilde{\varsigma}^{(\beta)} = [\tilde{P}^{(\alpha)}_{ijkl}, \tilde{P}^{(\alpha\beta)}_{ijkl}, \tilde{M}^{(\alpha)}_{ijkl}, \cdots]$. Analogously, a set for the second order zero eigenmode coefficient tensors is defined, and corresponds to the set of coefficient tensors where, both α and β has degraded. $\hat{\tilde{\varsigma}}^{(\beta\nu)} = [\hat{\tilde{P}}^{(\alpha)}_{ijkl}, \hat{\tilde{P}}^{(\alpha\beta)}_{ijkl}, \hat{\tilde{M}}^{(\alpha)}_{ijkl}, \cdots]$.

Finally, a metric in which to select the correct set of coefficient tensors needs to be defined. The trivial way is to utilize the information from the phase damage, $\omega^{(\alpha)}$, if the phase damage values have achieved 1 or otherwise.

Let ς, correspond to the collection of all the coefficient tensors.

$$\varsigma = \begin{cases} \bar{\varsigma} & \text{if} \quad \omega^{(\alpha)} < 1 \quad \forall \alpha = 1,2,\ldots,n \\ \tilde{\varsigma}^{(\beta)} & \text{if} \quad \omega^{(\beta)} = 1; \quad \omega^{(\alpha)} < 1; \quad \alpha \neq \beta \\ \hat{\tilde{\varsigma}}^{(\beta\nu)} & \text{if} \quad \omega^{(\beta)} = \omega^{(\nu)} = 1; \quad \omega^{(\alpha)} < 1; \quad \alpha \neq \beta, \nu \\ \vdots & \end{cases} \tag{3.56}$$

A new tensor of elastic moduli, $\hat{L}^{(\alpha)}_{ijkl}$, which is related to phase damage is defined as:

$$\hat{L}^{(\alpha)}_{ijkl}(\mathbf{y}) = \begin{cases} L^{(\alpha)}_{ijkl} & \text{if} \quad \omega^{(\alpha)} < 1 \quad \forall \alpha = 1,2,\ldots,n \\ \iota L^{(\beta)}_{ijkl} & \text{if} \quad \omega^{(\beta)} = 1; \quad \omega^{(\alpha)} < 1; \quad \alpha \neq \beta \\ \iota L^{(\beta\nu)}_{ijkl} & \text{if} \quad \omega^{(\beta)} = \omega^{(\nu)} = 1; \quad \omega^{(\alpha)} < 1; \quad \alpha \neq \beta, \nu \\ \vdots & \end{cases} \tag{3.57}$$

where, $\iota \ll 1$, is a very small, positive scaling constant. When $\iota = 1$, the original tensor of elastic moduli defined in $\Theta^{(\alpha)}$, is recovered. This concludes the process behind generating these multiple sets (i.e., first order, second order, ect.) of coefficient tensors corresponding to these zero mode eigenstrains.

The consideration of these modified 'zero mode' impotent eigenstrains are a novel contribution because multiple sets of coefficient tensors are computed *a-prior* to the macroscale analysis. Thus, they are computed one time and stored away for later use during the macroscale stress update of the ROM analysis, as opposed to recomputing the coefficient tensors which is computationally prohibitive.

3.5 Damage Evolution Model

The evolution of the inelastic strain is based on the thermodynamic theory of irreversible processes with internal state variables and is modeled using a scalar continuum

damage mechanics model:

$$\mu_{ij}^{(\alpha)} = \omega^{(\alpha)} \varepsilon_{ij}^{(\alpha)} \tag{3.58}$$

in which, $\omega^{(\alpha)} \in [0,1)$ is the damage variable with $\omega^{(\alpha)} = 0$ and $\omega^{(\alpha)} \to 1$ indicate the states of no damage and complete loss of load carrying capacity within part $\Theta^{(\alpha)}$.
The evolution of the damage variable follows:

$$\omega^{(\alpha)}(\mathbf{x},t) = \Phi\left(\kappa^{(\alpha)}(\mathbf{x},t)\right); \quad \frac{\partial \Phi\left(\kappa^{(\alpha)}\right)}{\partial \kappa^{(\alpha)}} \geq 0 \tag{3.59}$$

$$\kappa^{(\alpha)}(\mathbf{x},t) = \max\left\{ \hat{\upsilon}_{nl}^{(\alpha)}(\mathbf{x},\tau) \,\middle|\, \tau \leq t \right\}. \tag{3.60}$$

To help define the strain driver for the damage model, critical plane theory provides some insight for a better understanding of the principal causes of these many failure mechanism in structures. Some of these failures can be attributed to complex geometrical shapes of engineering structures and components (i.e. aircrafts, vehicles, axles and rotating disk) which result in complex multiaxial stress-strain states instead of simplified uniaxial loadings. In critical plane approaches, the basic postulate is that cracks initiate and grow on certain planes and that the normal strains to those planes help to propagate the crack growth. Although this gives us a physical interpretation of how the fatigue damage accumulation process works, similar principals can be applied to understand how failure in continuum damage occurs. There are several multiaxial fatigue theories to predict fatigue life originally proposed by Brown and Miller [52], the approach was modified by Fatemi and Socie with additional hardening parameters [53], the stress and strain models using Tresca and Mises criteria were proposed by Kandil et al. [54] and current research conducted by Liu and Mahadevan [55] investigates high cycle fatigue predictions. Utilizing the general form for the effective strain amplitude based on von Mises to describe the nominal normal and shear strains, a slight modification to the equivalent principal strains definition found in any linear elastic mechanics book can be used. This modified scaling parameter is on the

maximum shear strain amplitude and does not negate the contributions from the maximum normal strains in the other directions.

To define the equivalent strain measure $\upsilon_{ph}^{(\alpha)}$, a modified principal strain definition in terms of strains is utilized and has the following form:

$$\upsilon_{ph}^{(\alpha)} = \frac{\varepsilon_{11}+\varepsilon_{22}}{2} \pm \sqrt{\left(\frac{\varepsilon_{11}-\varepsilon_{22}}{2}\right)^2 + (k\varepsilon_{12})^2} \tag{3.61}$$

where, ε_{11}, ε_{22}, and ε_{12} are the x and y normal strain components and the xy is the shear component. k is a material parameter which scales the shear term, when $k \to 1$ implies principle strains as the equivalent strain measure. To investigate the influence of k on the model please refer to the Appendix A for details. Following the modified principle strain definition, the modified strains are computed and used in the Mazar's model:

$$\hat{\upsilon}_{ph}^{(\alpha)} = \sqrt{\sum_{i=1}^{2} \left\langle \upsilon_{ph_{(i)}}^{(\alpha)} \right\rangle_+^2} \tag{3.62}$$

$\hat{\upsilon}_{ph}^{(\alpha)}$ is the damage equivalent strain based on Mazar's model [56]. The positive part of Eq. 3.62 is used as the driver in the nonlocal damage model. When the modified equivalent strain reaches a threshold, damage within the material is activated and the material loses strength due to the damage accumulation. The nonlocal damage equivalent strains are expressed as:

$$\hat{\upsilon}_{nl}^{(\alpha)}(\mathbf{y},\hat{\mathbf{y}}) = \frac{\int_\Theta \lambda(\mathbf{y},\hat{\mathbf{y}})\hat{\upsilon}_{ph}^{(\alpha)}(\mathbf{y},\hat{\mathbf{y}})\,d\hat{y}}{\int_\Theta \lambda(\mathbf{y},\hat{\mathbf{y}})\,d\hat{\mathbf{y}}} \tag{3.63}$$

The evolution of phase damage as a function of the phase deformation function follows the arctangent law [1]

$$\Phi^{(\alpha)} = \frac{atan\left(a^{(\alpha)}\kappa^{(\alpha)}(\mathbf{x},t) - b^{(\alpha)}\right) + atan\left(b^{(\alpha)}\right)}{\pi/2 + atan\left(b^{(\alpha)}\right)} \tag{3.64}$$

in which, $a^{(\alpha)}$ and $b^{(\beta)}$ are material parameters.

3.6 Computational Aspects

To accurately capture the overall behavior of the composite material, it is necessary to have the correct implementation of the reduced order model. The implementation of the reduced order model is conducted in two stages where the first stage involves the decomposition of elastic and inelastic strains which allows for the precomputations of localization operators, coefficient tensors, influence functions *a priori* to the nonlinear analysis. The second stage is the macroscale stress update during the nonlinear analysis.

3.6.1 Numerical Evaluation of the Reduced-Order Model

The evaluation of the reduced order model for the microscale boundary value problem involves updating the macroscopic stress at a macro material point. A brief outline of the macroscopic stress update procedure will be provided below.

Given: The overall macroscopic strain, ${}_t\bar{\varepsilon}_{ij}$ is provided at a material point and time; the increment of the overall strain, $\Delta_t\bar{\varepsilon}_{ij}$; the phase damage variables, ${}_t\omega_{\text{ph}}^{(\alpha)}$; and the damage induced inelastic strains, ${}_t\mu_{ij}^{(\alpha)}$. The previous and current increments are denote by ${}_t\diamond$ and ${}_{t+1}\diamond$, respectively. When referring to the left subscript of current increment, it will be neglected in the writing for simplicity.

Compute: The current values (at time: $t+\Delta t$) of the overall macroscopic stress, $\bar{\sigma}_{ij}$; the current phase damage variables, $\omega_{\text{ph}}^{(\alpha)}$; and the current damage induced inelastic strains, $\mu_{ij}^{(\alpha)}$.

$$\mathbf{d} = \left\{ \boldsymbol{\mu}^{(1)}, ..., \boldsymbol{\mu}^{(n)} \right\}^T \tag{3.65}$$

The discrete system of nonlinear equations, Ψ, are defined based on reduced order model as:

$$\Psi(\mathbf{d}) = \mathbf{K}\left(\omega_{\text{ph}}^{(\alpha)}\right)\mathbf{d} + \mathbf{f}\left(\omega_{\text{ph}}^{(\alpha)}; \bar{\varepsilon}_{ij}\right) = 0 \tag{3.66}$$

where, $\mathbf{f}$ is the contribution of the force vector.

$$\mathbf{K} = \left[\begin{array}{c} \mathbf{K}_{PP}(\omega_{ph}^{(\alpha)}) \end{array} \right] \tag{3.67}$$

and

$$\mathbf{K}_{PP} = \left[\begin{array}{cccc} I_{ijkl} - P_{ijkl}^{(11)}\omega_{ph}^{(1)} & -P_{ijkl}^{(12)}\omega_{ph}^{(1)} & \cdots & -P_{ijkl}^{(1n)}\omega_{ph}^{(1)} \\ -P_{ijkl}^{(21)}\omega_{ph}^{(2)} & I_{ijkl} - P_{ijkl}^{(22)}\omega_{ph}^{(2)} & \cdots & -P_{ijkl}^{(2n)}\omega_{ph}^{(2)} \\ \vdots & \vdots & \ddots & \vdots \\ -P_{ijkl}^{(n1)}\omega_{ph}^{(n)} & -P_{ijkl}^{(n2)}\omega_{ph}^{(n)} & \cdots & I_{ijkl} - P_{ijkl}^{(nn)}\omega_{ph}^{(n)} \end{array} \right] \tag{3.68}$$

$\mathbf{K}$ is an *unsymmetric* matrix and the solution of $\Psi = 0$ is evaluated by unsymmetric nonlinear solvers. The force vector, $\mathbf{f}$ is defined as

$$\mathbf{f} = \left\{ A_{ijkl}^{(1)}\omega_{ph}^{(1)}, A_{ijkl}^{(2)}\omega_{ph}^{(2)}, \cdots, A_{ijkl}^{(n)}\omega_{ph}^{(n)} \right\}^T \bar{\varepsilon}_{kl} \tag{3.69}$$

The computational algorithm to evaluate the reduced order model is outlined in Box 1. (Step 1) The algorithm is initiated by imposing the overall strain, ${}_t\bar{\varepsilon}_{ij}$, on the reduced order domain. The next strain increment is calculated at $(t + \Delta t)$ and (Step 2 and 3) Newton's method is initialized and employed to find the root of the nonlinear eigendeformation vector, $\mathbf{d}$. There are several nonlinear solvers that can be utilized at this step, but Newton's solver is used because it is relatively stable and provides quadratic convergence so long as the step size is not too large. The Jacobian is calculated and the approximation for ${}^{k+1}\mathbf{d}$ is made. (Step 4) The analysis will iteratively march along until convergence is satisfied before moving to the next step. The macroscopic stress is calculated and the analysis proceeds until the end of the algorithm. $\Delta_t\bar{\varepsilon}_{ij}$

1. Update the macroscopic strains: $\bar{\varepsilon}_{ij} = {}_t\bar{\varepsilon}_{ij} + \Delta\bar{\varepsilon}_{ij}$
2. Utilize Newton's method to solve Eqn. 3.66

$$ {}^{k+1}\mathbf{d} = {}^{k}\mathbf{d} - \left(\frac{\partial \Psi}{\partial \mathbf{d}}\right)|^{-1}_{{}^{k}\mathbf{d}} \Psi|_{{}^{k}\mathbf{d}} \tag{3.70} $$

3. Initialize Newton's method by setting $k = 0$, ${}^{k}\mathbf{d} = {}_t\mathbf{d}$, ${}^{k}\omega^{(\alpha)}_{ph} = {}_t\omega^{(\alpha)}_{ph}$.
4. Loop over the iterations k until convergence:
   (a) Compute ${}^{k}\mathbf{K}, {}^{k}\mathbf{f}$, and $\left(\frac{\partial \Psi}{\partial \mathbf{d}}\right)|^{-1}_{{}^{k}\mathbf{d}}$.
   (b) Evaluate Eqn. 3.70 to obtain ${}^{k+1}\mathbf{d}$.
   (c) $k \leftarrow k+1$
5. Compute the macroscopic stress $\bar{\sigma}_{ij}$ utilizing Eqn. 3.32.
   (a) Exit the algorithm

   End iteration loop

Box 1: The stress update algorithm for evaluation of the reduced order model.

3.6.2 Macroscopic tangent moduli

In this section, a closed form expression for the macroscopic tangent moduli, $\mathcal{L}_{ijkl}$ is derived and the field values at the current and previous time steps as noted in Section 3.3.1 are recorded. In Section 3.4, the macroscopic stress was expressed as:

$$ \bar{\sigma}_{ij}(\mathbf{x},t) = \bar{L}_{ijkl}\bar{\varepsilon}_{kl}(\mathbf{x},t) + \sum_{\alpha=1}^{n} \bar{M}^{(\alpha)}_{ijkl}\mu^{(\alpha)}_{kl}(\mathbf{x},t) \tag{3.71} $$

where the coefficient tensors, $\bar{L}_{ijkl}$ and $\bar{M}^{(\alpha)}_{ijkl}$ are independent of the macroscopic strain, $\bar{\varepsilon}_{kl}(\mathbf{x},t)$. The closed form of $\mathcal{L}_{ijkl}$ is determined by differentiating Eq. 3.32 with respect to $\bar{\varepsilon}_{kl}(\mathbf{x},t)$:

$$ \mathcal{L}_{ijkl} = \frac{\bar{\sigma}_{ij}}{\bar{\varepsilon}_{kl}} = \bar{L}_{ijkl} + \sum_{\alpha=1}^{n} \bar{M}^{(\alpha)}_{ijmn}\frac{\partial \mu^{(\alpha)}_{mn}}{\partial \bar{\varepsilon}_{kl}} \tag{3.72} $$

Thus, to evaluate $\frac{\partial \mathbf{d}}{\partial \bar{\varepsilon}_{kl}}$, refer back to the discrete system in Eq. 3.66:

$$\hat{\Psi}(\mathbf{d}) = \mathbf{K}(\mathbf{d})\,\mathbf{d} - \mathbf{f}\left(\mathbf{d}; \bar{\varepsilon}_{ij}\right) = 0 \tag{3.73}$$

and taking derivatives of the above expression with respect to $\bar{\varepsilon}_{kl}(\mathbf{x},t)$ and using chain rule yields:

$$\frac{\partial \mathbf{d}}{\partial \bar{\varepsilon}_{kl}} = \mathcal{C}^{-1}\frac{\partial \mathbf{f}}{\partial \bar{\varepsilon}_{kl}}, \tag{3.74}$$

where,

$$\mathcal{C} = \frac{\partial \hat{\Psi}}{\partial \mathbf{d}} = \frac{\partial \mathbf{K}}{\partial \mathbf{d}}\mathbf{d} + \mathbf{K} - \frac{\partial \mathbf{f}}{\partial \mathbf{d}} \tag{3.75}$$

the expression for $\frac{\partial \mathbf{f}}{\partial \bar{\varepsilon}_{kl}}$ is obtained trivially from Eqn. 3.69:

$$\mathbf{f} = \left\{A^{(1)}_{ijkl}\omega^{(1)}_{ph}, A^{(2)}_{ijkl}\omega^{(2)}_{ph}, \cdots, A^{(n)}_{ijkl}\omega^{(n)}_{ph}\right\}^T. \tag{3.76}$$

Differentiating the force vector, $\mathbf{f}$ with respect to the vector of state variables, $\mathbf{d}$ and using chain rule yields:

$$\frac{\partial \mathbf{f}}{\partial \mathbf{d}} = \sum_{\alpha=1}^{n} \frac{\partial \mathbf{f}}{\partial \omega^{(\alpha)}_{ph}} \frac{\partial \omega^{(\alpha)}_{ph}}{\partial \mathbf{d}}; \tag{3.77}$$

where,

$$\frac{\partial \omega^{(\alpha)}_{ph}}{\partial \mathbf{d}} = \frac{\partial \omega^{(\alpha)}_{ph}}{\partial \kappa^{(\alpha)}_{ph}} \frac{\partial \kappa^{(\alpha)}_{ph}}{\partial \nu^{(\alpha)}_{ph}} \frac{\partial \nu^{(\alpha)}_{ph}}{\partial \varepsilon^{(\alpha)}} \frac{\partial \varepsilon^{(\alpha)}}{\partial \tilde{\varepsilon}^{(\alpha)}} \frac{\partial \tilde{\varepsilon}^{(\alpha)}}{\partial \mathbf{d}}. \tag{3.78}$$

The expression for $\frac{\partial \mathbf{f}}{\partial \omega^{(\alpha)}_{ph}}$ may be calculated by differentiating Eq. 3.69 with respect to the phase damage variable, $\omega^{(\alpha)}_{ph}$ yields:

$$\frac{\partial \mathbf{f}}{\partial \omega^{(\alpha)}_{ph}} = \left\{0, \cdots, 0, A^{(\alpha)}_{ij}\bar{\varepsilon}_j, 0, \cdots, 0\right\}^T. \tag{3.79}$$

$\frac{\partial \omega_{ph}^{(\alpha)}}{\partial \kappa_{ph}^{(\alpha)}}$ is calculated by differentiating Eqn. 3.64

$$\frac{\partial \omega_{ph}^{(\alpha)}}{\partial \kappa_{ph}^{(\alpha)}} = \frac{a_{ph}^{(\alpha)}}{\left[\pi/2 + atan(b_{ph}^{(\alpha)}\right]\left[1 + (a_{ph}^{(\alpha)}\kappa_{ph}^{(\alpha)} - b_{ph}^{(\alpha)})^2\right]}. \tag{3.80}$$

$\frac{\partial \kappa_{ph}^{(\alpha)}}{\partial \nu_{ph}^{(\alpha)}} = 1$ during damage accumulation and vanishes if their is no damage in the current step k. $\frac{\partial \nu_{ph}^{(\alpha)}}{\partial \varepsilon^{(\alpha)}}$ is obtained by differentiating Eq. 3.61 with respect to the total strain, consequently, there are three strain components to consider. The derivatives components of the modified equivalent strains are obtained as:

$$\frac{\partial \nu_{ph}^{(\alpha)}}{\partial \varepsilon^{(\alpha)}} = \frac{\partial \nu_{ph}^{(\alpha)}}{\partial \varepsilon_{11}^{(\alpha)}} + \frac{\partial \nu_{ph}^{(\alpha)}}{\partial \varepsilon_{22}^{(\alpha)}} + \frac{\partial \nu_{ph}^{(\alpha)}}{\partial \varepsilon_{12}^{(\alpha)}} \tag{3.81}$$

$$\frac{\partial \nu_{ph}^{(\alpha)}}{\partial \varepsilon_{11}^{(\alpha)}} = \frac{1}{2} \pm \frac{\varepsilon_{11} - \varepsilon_{22}}{4} \frac{1}{\sqrt{\left(\frac{\varepsilon_{11}-\varepsilon_{22}}{2}\right)^2 + (k\varepsilon_{12})^2}} \tag{3.82}$$

$$\frac{\partial \nu_{ph}^{(\alpha)}}{\partial \varepsilon_{22}^{(\alpha)}} = \frac{1}{2} \pm \frac{\varepsilon_{11} - \varepsilon_{22}}{4} \frac{1}{\sqrt{\left(\frac{\varepsilon_{11}-\varepsilon_{22}}{2}\right)^2 + (k\varepsilon_{12})^2}} \tag{3.83}$$

$$\frac{\partial \nu_{ph}^{(\alpha)}}{\partial \varepsilon_{12}^{(\alpha)}} = \pm \frac{k^2 \varepsilon_{12}}{4} \frac{1}{\sqrt{\left(\frac{\varepsilon_{11}-\varepsilon_{22}}{2}\right)^2 + (k\varepsilon_{12})^2}}. \tag{3.84}$$

$\frac{\partial \varepsilon^{(\alpha)}}{\partial \tilde{\varepsilon}^{(\alpha)}}$ is obtained by taking the derivative with respect to the strain field, hence it is equal to the identity tensor. The phase average damage induced strains, $\tilde{\varepsilon}^{(\alpha)}$ can be expressed in terms of damage induced strains, which is given below:

$$\tilde{\varepsilon}_{ij}^{(\alpha)} = \sum_{\alpha=1}^{n} P_{ijkl}^{(\alpha\beta)} \mu_{kl}^{(\alpha)}(\mathbf{x}, t). \tag{3.85}$$

The derivative of $\tilde{\varepsilon}_{ij}^{(\alpha)}$ with respect to $\mathbf{d}$ yields:

$$\frac{\partial \tilde{\boldsymbol{\varepsilon}}^{(\alpha)}}{\partial \mathbf{d}} = \left\{ P_{ijkl}^{(\alpha 1)} \quad P_{ijkl}^{(\alpha 2)} \quad \cdots \quad P_{ijkl}^{(\alpha n)} \right\}, \tag{3.86}$$

this final derivative completes the evaluation of $\frac{\partial \mathbf{f}}{\partial \mathbf{d}}$. The $\mathbf{K}$ matrix is a function of the phase damage variables, $\omega_{ph}^{(\alpha)}$ as displayed in Eqns. 3.66-3.68.

$$\frac{\partial \mathbf{K}}{\partial \mathbf{d}} = \sum_{\alpha=1}^{n} \frac{\partial \mathbf{K}}{\partial \omega_{ph}^{(\alpha)}} \frac{\partial \omega_{ph}^{(\alpha)}}{\partial \mathbf{d}}, \tag{3.87}$$

and it has nonzero components when evaluating the derivative of $\mathbf{K}$ with respect to damage variable, $\frac{\partial \mathbf{K}_{PP}}{\partial \omega_{ph}^{(\alpha)}}$, hence it has the form below:

$$\frac{\partial \mathbf{K}_{PP}}{\partial \omega_{ph}^{(\alpha)}} = \begin{bmatrix} 0 & 0 & \cdots & 0 \\ \vdots & \vdots & \ddots & \vdots \\ 0 & 0 & \cdots & 0 \\ -P_{ijkl}^{(\alpha 1)} & -P_{ijkl}^{(\alpha 2)} & \cdots & -P_{ijkl}^{(\alpha n)} \\ 0 & 0 & \cdots & 0 \\ \vdots & \vdots & \ddots & \vdots \\ 0 & 0 & \cdots & 0 \end{bmatrix}. \tag{3.88}$$

3.6.3 Implementation strategy

Figure 3.4 gives the computational framework for computing the macroscopic stress in the reduced order analysis. One advantage of using computational homogenization is that the methodology is valid for a spectrum of different material properties and microstructures. The user only needs to supply the geometry of the microstructure, the material properties of the composite material and the failure paths which forms the reduced basis for the system. The CoefTenseCompute program will then evaluate the elastic boundary

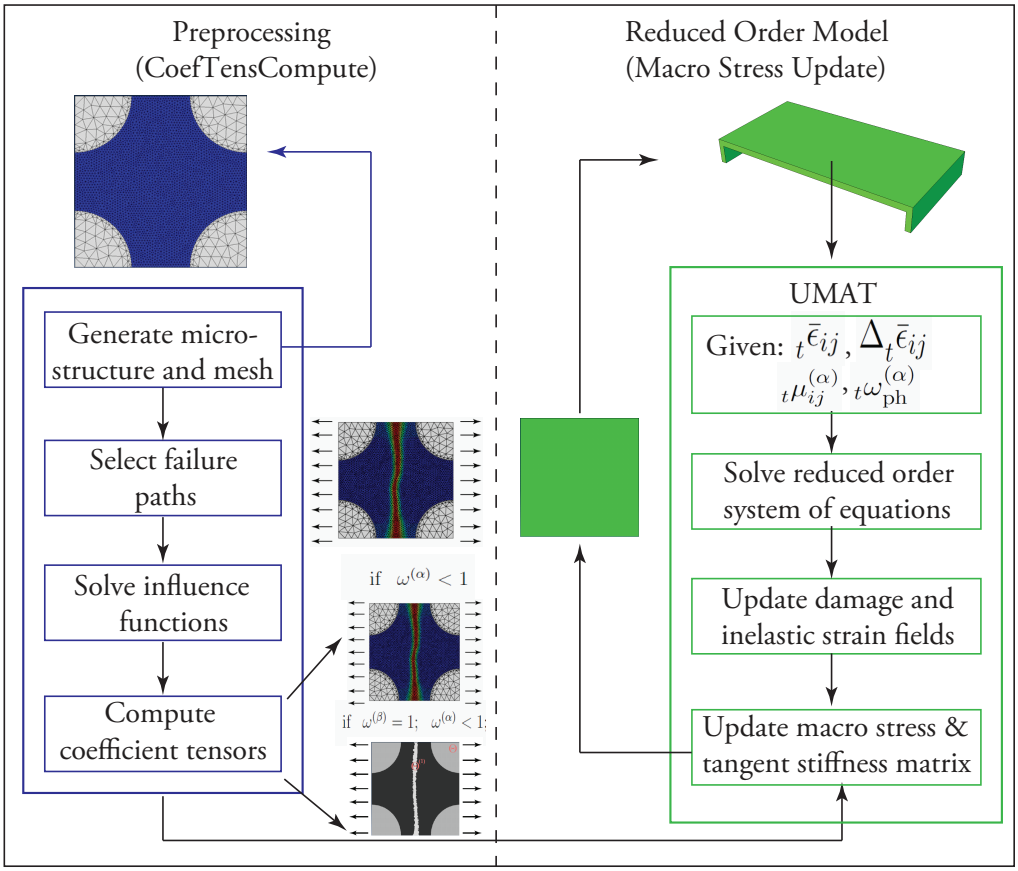

Figure 3.4: Computational framework for solving reduced order model.

value problem for the elastic influence functions and then solve for the phase influence functions before ultimately outputting the coefficient tensors corresponding to the reduced order model. The coefficient tensors are inputs for the calculation of the macroscale stress. An important remark to note is the macroscale geometry is not limited and is valid for any arbitrary geometry once the coefficient tensors are generated. Hence, the user can evaluate a series of different macroscale domains as necessary. The macroscale analysis is implemented through a user supplied subroutine (i.e., UMAT) and it solves the system of nonlinear equations in the ROM and calculates the updated macroscopic stress.

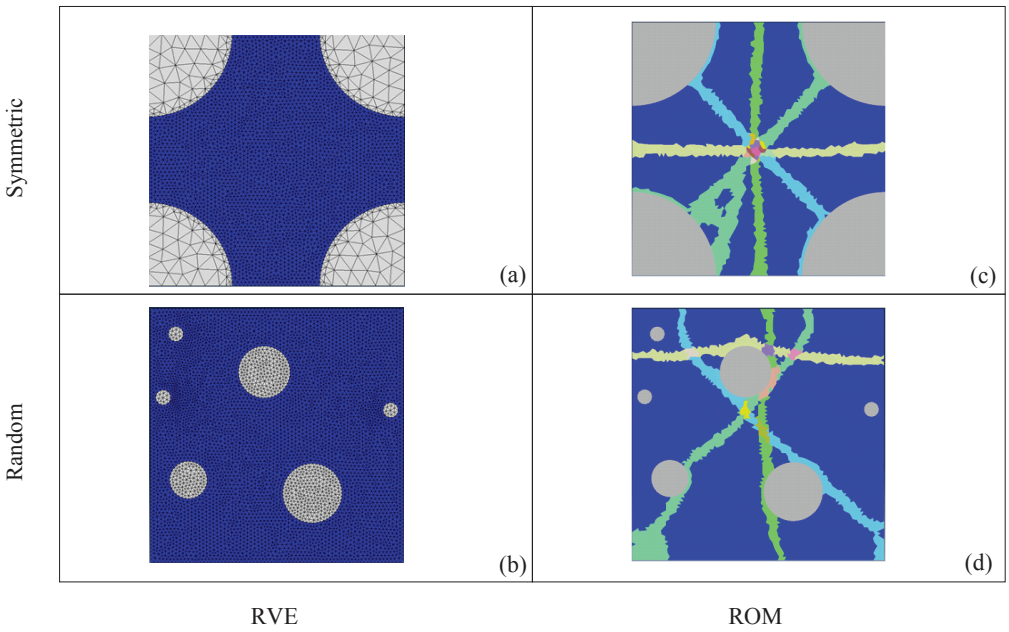

Figure 3.5: Symmetric and random microscopic structures and ROMs

3.7 Numerical Examples

Numerical verification experiments were conducted to assess the capabilities of the proposed reduced order models compared to the direct finite element simulations. The analysis is conducted by considering a unidirectional fiber reinforced matrix microstructure with geometry and discretization as shown in Fig. 3.5a-b, for a symmetric and random fiber microstructure, respectively. The single element ROM for each case is also shown with parts as defined in Section 3.4.2, and there corresponding geometry is shown in Fig. 3.5c-d, for the symmetric and random microstructures. The verification study consists of: (1) analyzing the resolved RVE response and comparing with the ROM predictions, and (2) analyzing a fully resolved macroscale beam problem and assessing the performance and capabilities of the reduced order model in capturing the overall macroscopic failure response.

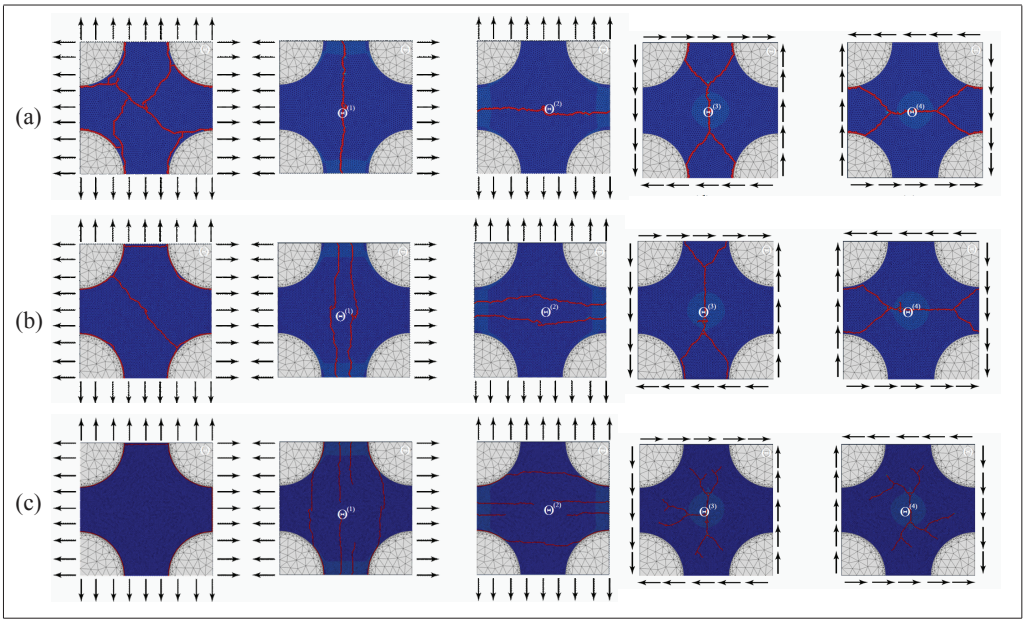

Figure 3.6: Symmetric microstructure with local model (a) coarse mesh: 6,698 elements; (b) medium mesh: 11,242 elements; (c) fine mesh: 24,848 elements.

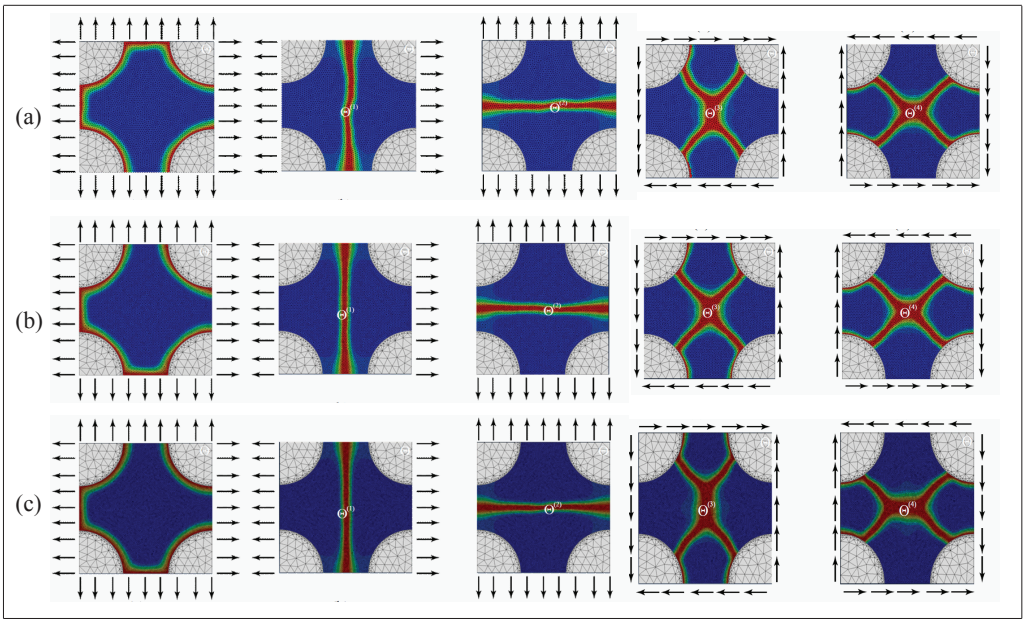

Figure 3.7: Symmetric microstructure with nonlocal model (a) coarse mesh: 6,698 elements; (b) medium mesh: 11,242 elements; (c) fine mesh: 24,848 elements.

3.7.1 Preliminary RVE investigations

Preliminary mesh studies were conducted during the verification stage on the local model as well as the nonlocal model for the determination of the appropriate characteristic length as shown in Fig. 3.6 and Fig. 3.7. The local damage models used during this preliminary verification study were similar to the one defined in [4]. Failure regions under various loadings using local and nonlocal damage evolution are shown in Figs. 3.6 and 3.7, respectively. A mesh size of coarse (Fig. 3.6a), medium (Fig. 3.6b), and fine (Fig. 3.6c) were considered. It was observed in the analysis with the local damage model, that the failure strains localize in single element wide regions, rendering the analysis highly mesh dependent. As the mesh is refined, the potential crack paths do not visually converge to the same failure path, instead multiple failure paths began to activate. It was also observed from the load-displacement curves that both the peak load and the total dissipated energy decrease as the mesh is refined. Mesh dependency of local damage models are very well understood in the literature [57, 58, 59], hence the need for a nonlocal formulation with a characteristic length larger than a single element to be introduced at the microstructural scale. Fig. 3.7 shows the effect of introducing a length scale into the nonlocal damage model formulation. As the mesh is refined, the potential failure crack paths remain unchanged and the mesh dependency is mitigated. The load-displacement curves for all the nonlocal mesh refinements exhibited the same peak load. *One remark:* The load-displacement curves corresponding to the local and nonlocal models are not shown since this phenomena is well documented in the literature, for the purposes of the preliminary mesh studies, it was sufficient enough to demonstrate the mesh dependency as shown in Fig. 3.6 and Fig. 3.7.

3.7.2 RVE analysis

Numerical verification analyses were conducted on the resolved RVE microstructures shown in Figs. 3.5a-b to identify failure paths and corresponding ROM parts as seen in

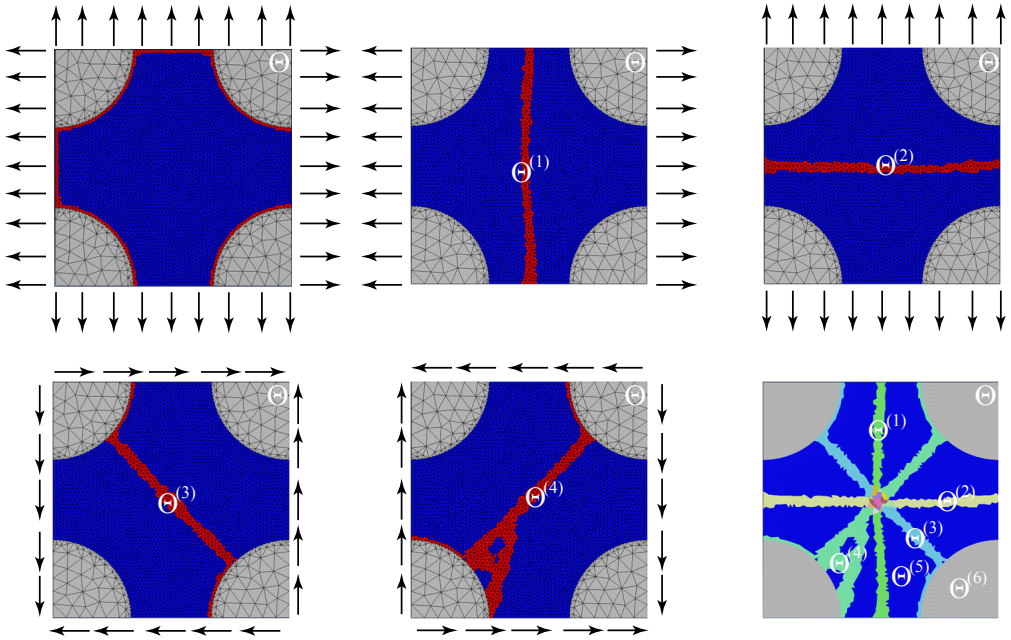

Figure 3.8: The partitioning and model reduction strategy. RVE failure profiles are shown when subjected to (a) uniform biaxial loading; (b) uniaxial in the lateral direction; (c) uniaxial in the vertical direction; (d) shear loading along the positive direction; (e) shear loading along the negative direction; (f) overlapping failure partition.

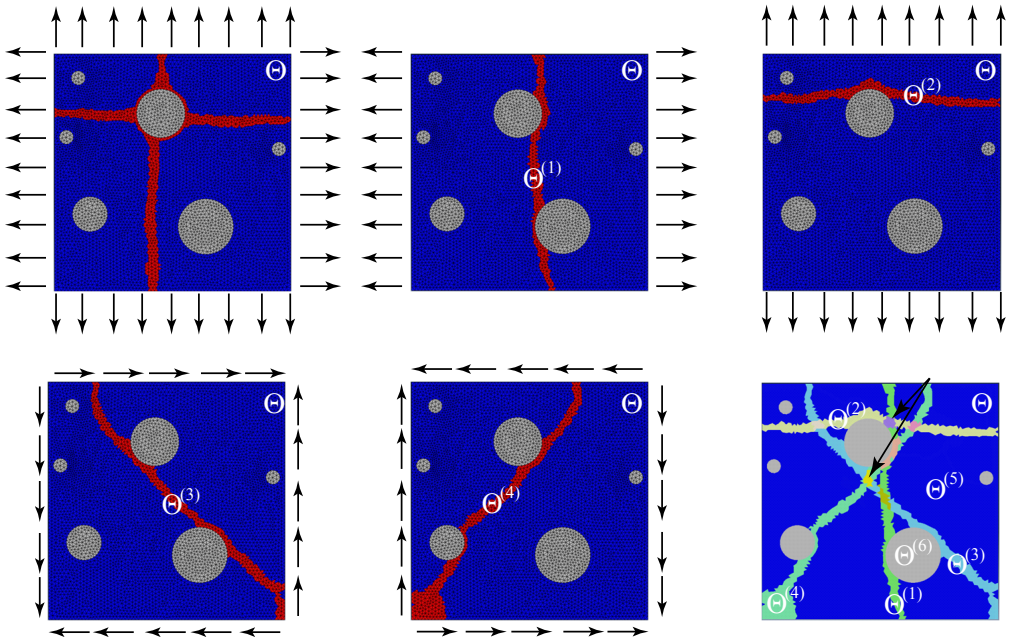

Figure 3.9: The partitioning and model reduction strategy. RVE failure profiles are shown when subjected to (a) uniform biaxial loading; (b) uniaxial in the lateral direction; (c) uniaxial in the vertical direction; (d) shear loading along the positive direction; (e) shear loading along the negative direction; (f) overlapping failure partition.

Figs. 3.8 and 3.9. The finite element discretization of the RVE for the symmetric microstructure and random microstructure consists of 6,698 and 11,241 triangular elements, respectively. The symmetric microstructure matrix and reinforcements are discretized using 6,240 and 458 elements. The random microstructure matrix and reinforcements are discretized using 10,072 and 1,169 elements. The ROM is discretized into non-overlapping and overlapping parts with model order (n=15 and n=6), respectively for the symmetric ROM. For the random ROM, the non-overlapping and overlapping parts have model order (n=12 and n=6), respectively. A single quadrilateral element of unit length is used to represent the macroscale domain for each of the two different microstructures. The volume fraction of the reinforcement within the RVE is 34% for the symmetric microstructure and 11% for the random microstructure. The characteristic length of the matrix material is taken to be 1/8 of the size of the RVE for both the microstructures.

3.7.3 RVE verifications

The performance of the reduced order models are assessed when the microstructures are subjected to the loading conditions shown in Figs. 3.8 and 3.9. The elastic modulus and the Poisson's ratio for the fiber are $E^{(f)}$= 400 GPa and $\nu^{(f)}$= 0.15; for the matrix they are $E^{(m)}$= 115 GPa and $\nu^{(m)}$=0.3. The fiber is taken to be linear elastic and the matrix is modeled using continuum damage mechanics with the material parameters of $a^{(m)}$= 10,000 and $b^{(m)}$= 45, from Eq. 3.64 and these parameters are also the same for each microstructure. The matrix phase is taken to have the same material properties in each part within the partition and the fiber reinforcement phase is taken to be in a single part. For the remainder of this section, a reduced order model is named based on the load cases employed in the identification step and the model order, n. T_i and S_{ij} denote uniaxial loading along the i-direction (i=x,y) and the shear loading along the ij-direction, respectively. P or N designation in front of the S_{ij} corresponds to positive or negative shear stress state, respectively.

The reference symmetric RVE direct finite element simulation is compared to the ROM

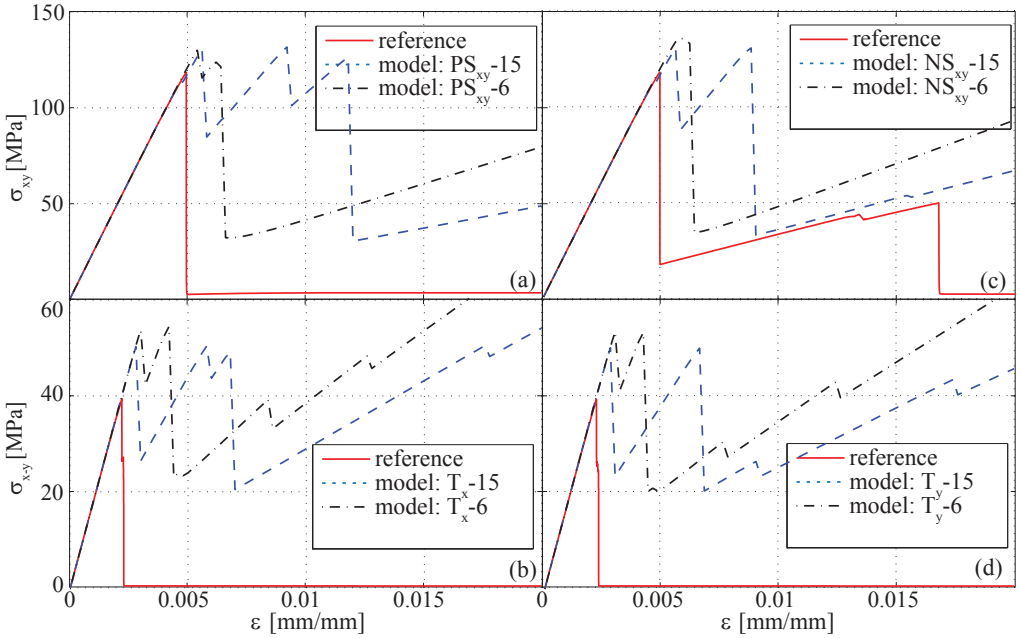

Figure 3.10: Stress-strain curves for the symmetric microstructure when subjected to (a) positive shear loading; (b) negative shear loading; (c) uniaxial in the lateral direction; (d) uniaxial in the vertical direction.

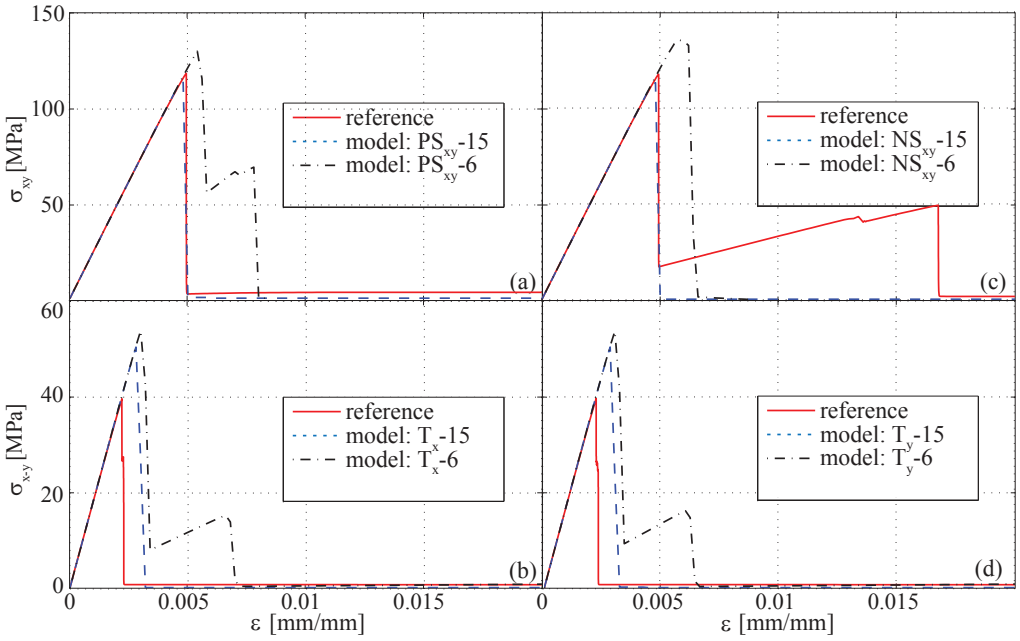

Figure 3.11: Stress-strain curves for the symmetric microstructure when subjected to (a) positive shear loading; (b) negative shear loading; (c) uniaxial in the lateral direction; (d) uniaxial in the vertical direction.

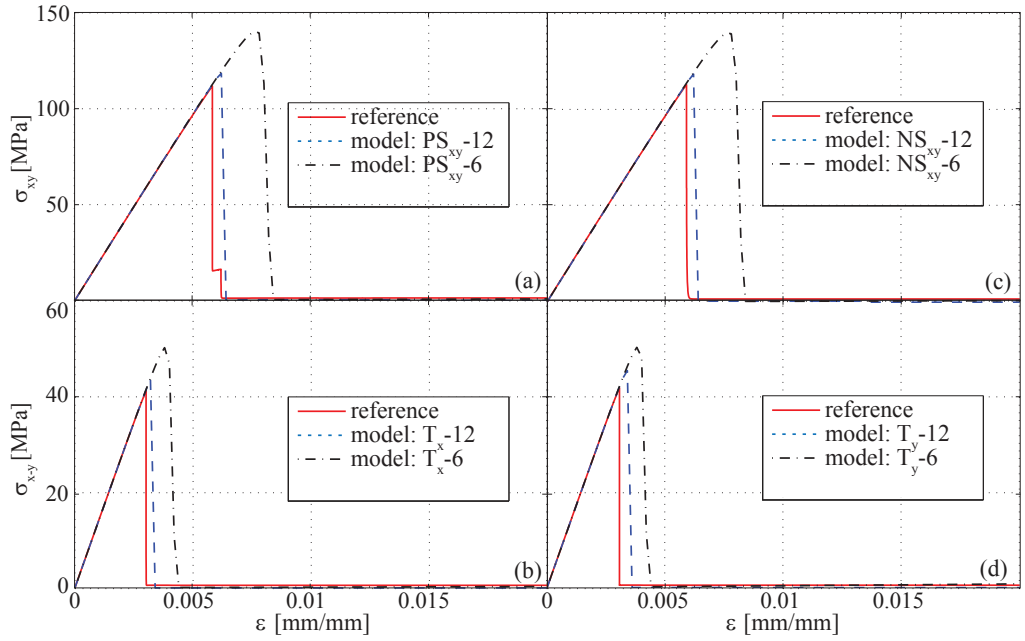

Figure 3.12: Stress-strain curves for the random microstructure when subjected to (a) positive shear loading; (b) negative shear loading; (c) uniaxial in the lateral direction; (d) uniaxial in the vertical direction.

with non-overlapping partition with model order, (n=15) and the ROM with overlapping partition with model order, (n=6). These results are summarized in Fig. 3.10. There are noticeable post failure residual stresses in all of the Fig. 3.10a-d and this phenomenon can be mitigated by utilizing the modified 'zero mode' impotent eigenstrains described in 3.4.3. The improved accuracy of the reduced order models (for the symmetric geometry) is summarized in Fig. 3.11. Utilizing the new zero mode eigenstrains minimizes the post failure spurious residual stresses. The post failure action of the brittle matrix material shows zero stress which indicates complete loss of load carrying capacity and shows that the ROM's can accurately handle the spurious stress behavior. In Fig. 3.11, as the number of parts increases, the stress-strain response of the reference simulation is more accurately captured but with additional computational effort. The symmetric microstructure ROM with model (n=15) has a larger system of nonlinear equations to solve than the (n=6) model. While the 6 part model sacrifices some of the accuracy, it is able to predict the failure envelope well while solving a smaller set of nonlinear equations. Fig. 3.12 shows the

random microstructure reference model in comparison with the ROM corresponding to the non-overlapping (n=12) and overlapping (n=6) ROM's. The ROM from Fig. 3.12 show reasonable agreement with the reference model for each of the loading scenarios. The effect of the spurious residual stresses for the random microstructure was not shown because the effect is similar to the results as shown in Fig. 3.10 for the symmetric microstructure and only the results for the zero mode analysis is shown here. The ROM models consistently over predict the peak stress before failure and this error can be improved by parameter scaling found in Ref. [60].

3.7.4 Crack propagation in a beam

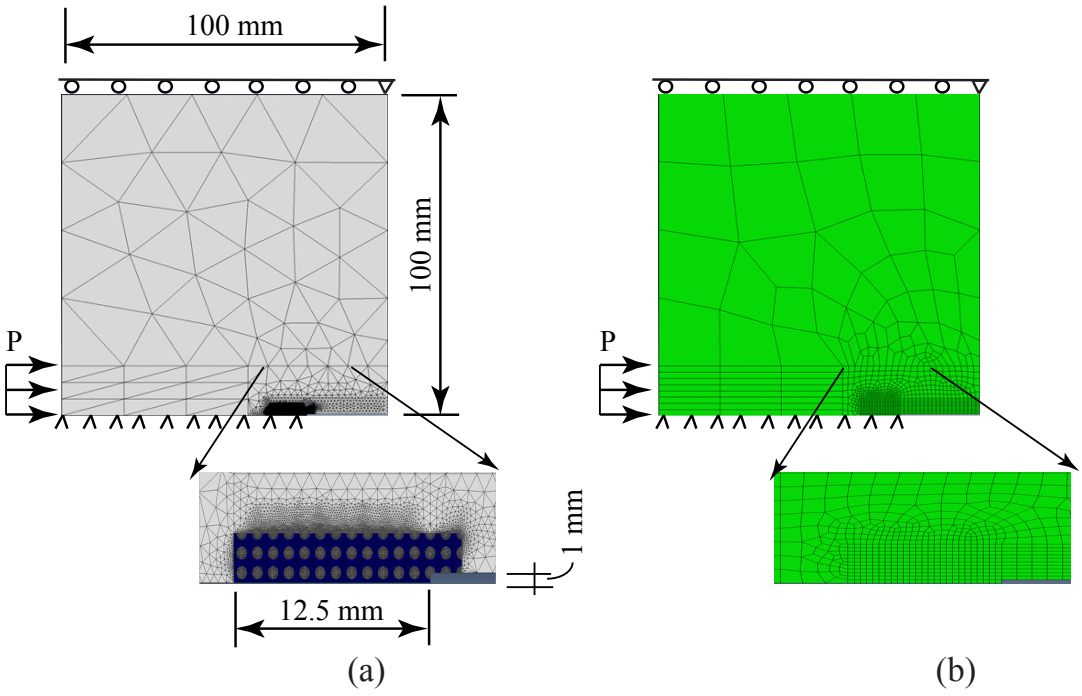

Figure 3.13: Geometry of the different macroscopic beam domains; (a) the periodic microstructure is resolved around the notch tip and (b) the ROM represents the homogenized response of the heterogeneous materials.

The notch beam is subjected to a tensile load and has been simulated using non-local damage continuum model and is shown in 3.13. Figures 3.13a-b are the geometries for the different macroscopic beam domains. In Fig. 3.13a, the periodic microstructure is resolved

around the notch tip and in Fig. 3.13b the ROM is used to represent the homogenized response of the heterogeneous material. The beams were subjected to a uniform displacement boundary condition, where $P = 0.06$ mm. The reference beam consists of 30,272 standard triangular elements and the ROM has 393 quadrilateral elements. The length of the beam is 200 mm and has a depth of 100 mm. Only half of the geometry is modeled using symmetric boundary conditions along the notch face. The dimension of the notch is 12.5 x 1 mm. The fibrous reinforcements are taken to be linear elastic and the matrix material is modeled using continuum damage mechanics. Numerical analyses were performed to determine the crack propagation response of the reference and multiscale ROM.

Figure 3.14 shows snapshots of reference and ROM crack length-applied displacement from tensile fracture onset. Fig. 3.14a shows the crack length of the reference model as compared to the ROM models T_x-15 and T_x-6 (non-overlapping and overlapping in Fig. 3.14b-c, respectively). It is shown that the overlapping model T_x-6 crack length is less than the reference, while non-overlapping model T_x-15 has a crack length greater than the reference at this applied displacement increment.

The rate of crack length grow is more pronounced in the ROM analysis as compared to the reference simulation as shown in Fig. 3.15. This error can be due to several issues. One source is the considerable amount of information that is lost during the model reduction formulation as compared to the direct finite element analysis. The representative volume element is assumed to be much smaller than the size of the overall macroscopic domain and this scale separation assumption is not always well pronounced. Another source of error lies in the fact that we are comparing a nonlocal damage model in the reference analysis to a local ROM, hence a length scale is present in the formulation of the reference model but the same does not exist in the ROM. Another source of error lies in the mesh resolution. ROM models for the non-overlapping and overlapping cases are highly mesh dependent and this is a direct artifact of utilizing local damage models and not having a characteristic length in the model. These are some of the errors that contribute to the crack length and

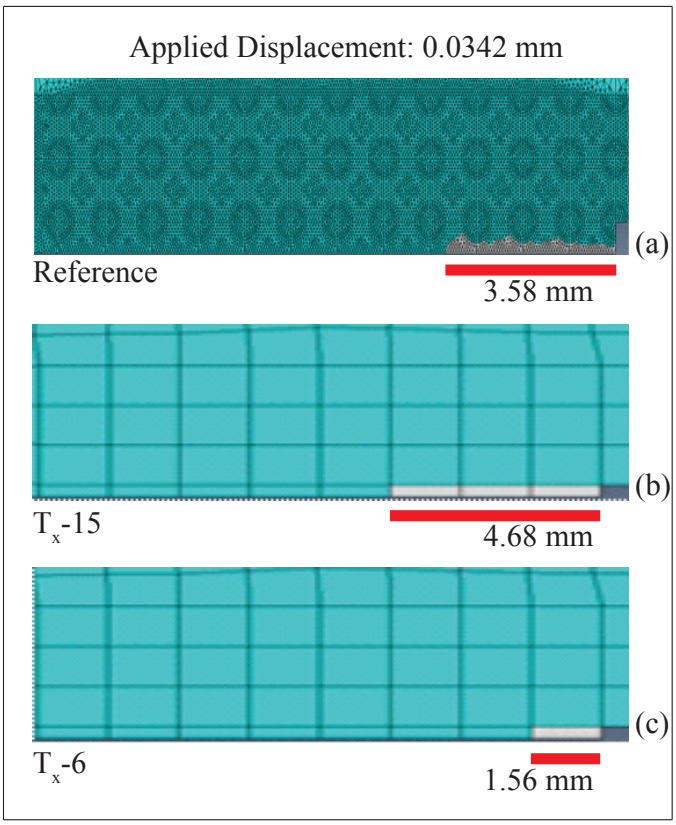

Figure 3.14: Snapshot of reference and ROMs crack length-applied displacement from tensile fracture onset at applied displacement of 0.0342 mm (a) reference, (b) T_x-15 and (c) T_x-6.

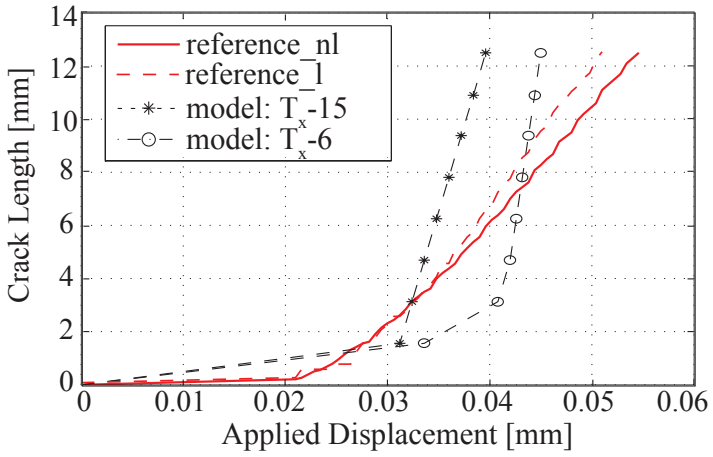

Figure 3.15: Reference and ROM crack length-applied displacement curves.

displacement curves not being perfectly aligned with the same crack rate. Incorporating a fracture mechanics model could also provide more information to better characterize the crack propagation rate and growth.

Chapter 4

CONCLUSION AND FUTURE WORK

4.1 Conclusion

This dissertation provided a computational framework for the formulation and implementation of an eigendeformation-based reduced order homogenization for characterizing the inelastic and failure response of composite materials. Numerical testing verified and assessed the performance characteristics of the proposed model against the direct finite element method. Detailed summaries of included work are presented below.

In chapter 2 a strategy for identifying optimal reduced order models for inelastic and failure response in heterogeneous materials was presented. The reduced order modeling approach in this study, is the eigendeformation-based reduced order homogenization method. The identification of the optimal reduced order model is posed as an integer optimization problem and the genetic algorithm method is used to evaluate the optimization problem. A series of numerical simulations were conducted to assess the performance of the identified reduced order models against the computational homogenization method, which considers full resolution of the material microstructure. Since the reduced order models are derived from the computational homogenization formulation in eigendeformation-based reduced order homogenization, the accuracy characteristics of the reduced order models are bounded by the computational homogenization method.

The reduced order models identified using the proposed methodology are able to accurately capture the failure response characteristics for a wide range of loading conditions in the investigations. The failure response using relatively small order models were found to be satisfactory. The errors do not monotonically reduce by increasing the model order. This is attributed to possible identification of reduced order models at local minima of the

objective function and the constraint imposed on high order models that preclude lower order models from being represented identically by the high order models in the model hierarchy.

While the proposed methodology is effective in identifying satisfactory reduced order models, some issues remain to be addressed. The parameter scaling for the materials that exhibit more complex microconstituent response characteristics call for a different identification approach than employed in this study. Constitutive models for more complex material behavior include multiple material parameters, which cannot be identified using the Nelder-Mead simplex method. The increase in computational complexity of the identification problem when the material microstructure is highly resolved remains outstanding. When the microstructure is densely meshed, the search space for the identification problem becomes very large and the interrogation of the search space with the posed integer optimization problem is computationally exhaustive. The reduction of the search space for the reduced order models is critical for highly resolved material microstructures.

Chapter 3 provided the formulation and implementation for reduced order model using eigendeformation based reduced order homogenization for modeling the failure of heterogeneous materials with overlapping failure paths. The macroscale and microscale boundary value problems were expanded using asymptotics and the system is evaluated in terms of transformation influence functions. The evaluation of the influence functions are dependent on the micro-structural partition, hence the problem may be posed as a system of nonlinear equations and is solved. Issues due to stress inclusion locking are alleviated by enhancing the constitutive laws which define the microphase reduced order model. First order (zero mode eigenstrains) coefficient tensors were generated for the analysis. The above idea is generalized to account for multiple sets of newly generated coefficient tensors (i.e., second order, and higher order) based on the combination of activated potential failure crack paths for a given loading condition. Computational efficiency is gained by allowing the potential failure paths to overlap. This effect results in a small number of a nonlinear system of

equations to be solved. Numerical verification experiments were conducted to access the capability of the RVE and a large scale beam problem was investigated.

4.2 Future Work

This dissertation focused on the computational framework for the formulation and implementation of an eigendeformation-based reduced order homogenization for characterizing the inelastic and failure response of composite materials. The main focus of future work will be the development and natural extension of this application using eigendeformation-based reduced order homogenization for modeling the failure of heterogeneous materials with overlapping failure paths in three dimensions. The development of the three dimensional framework will provide a more realistic approach to model laminate composites and analyze the response of the system. There are some conceptual difficulties that will arise when applying the proposed methodology, one major issue is upon failure of the material the crack has an infinite amount of degrees of freedom in which it can grow. Although it is impossible to capture all the different combinations of the crack growth throughout the constituent material, the problem will be limited to investigating dominate loading modes. Also these predictive failure models are particularly of interest because a lot of different failure mechanisms can occur within the microstructure of the composite material. There are several different failure mechanism and these include fiber buckling, fiber fracture, matrix failure and fiber matrix debonding [8].

The multiscale finite element analysis will be conducted using the commercial available finite element software Abaqus and the solution to the coupled microscale and macroscale problem will be calculated using a user material (UMAT) subroutine. The numerical investigations will be conducted on various composite laminates which have different orientations. Above in Fig. 4.1 is a schematic showing a sample laminate layup with the mesh aligned with the fiber direction of each ply. The nominal characteristic length for each ply

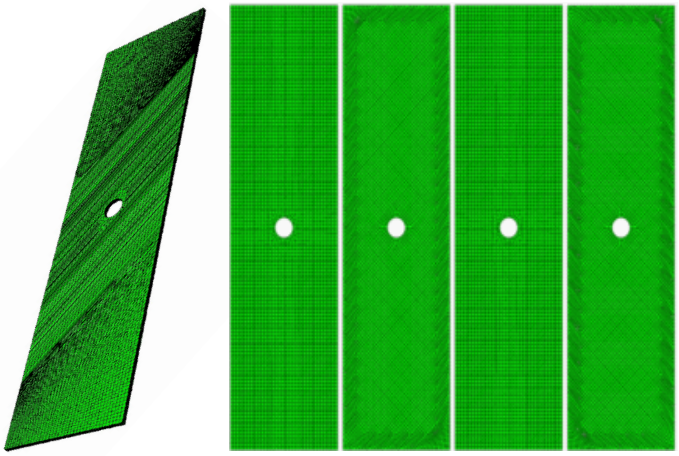

Figure 4.1: (a) Composite laminate lay-up with aligned mesh for the laminate plies oriented at $[0, 45, 90, -45]_{2s}$, which is (b-e), respectively.

is 1 mm in the in-plane direction of the ply and with one element per thickness of each layer. The laminate plies will be tied together using surface displacement constraints to ensure the composite deforms as a uniform structure.

The calculation of the nonlocal weights will take place during the pre-processing stage before numerical finite simulations are conducted to determine the laminate composite failure paths for the reduced order model. Careful consideration must be taken into account when determining these nonlocal weights because periodicity of the structure needs to be maintained when loading the microstructure. Since the microstructure is assumed to be locally periodic, this assumption must be validated.

Numerical verification analyses will be conducted by considering a unidirectional reinforced matrix microstructure with geometry, the discretization and the loading conditions are shown in Fig. 4.2. The finite element discretization of the unit cell consists of 351 tetrahedra. The matrix and the reinforcements are discretized using 251 and 98 elements, respectively. A unit cube discretized using a single hexahedral finite element constitutes the macroscale domain. The volume fraction of the reinforcement within the unit cell is 40%.

The unit cell will be subjected to range of loading conditions, some of which are shown

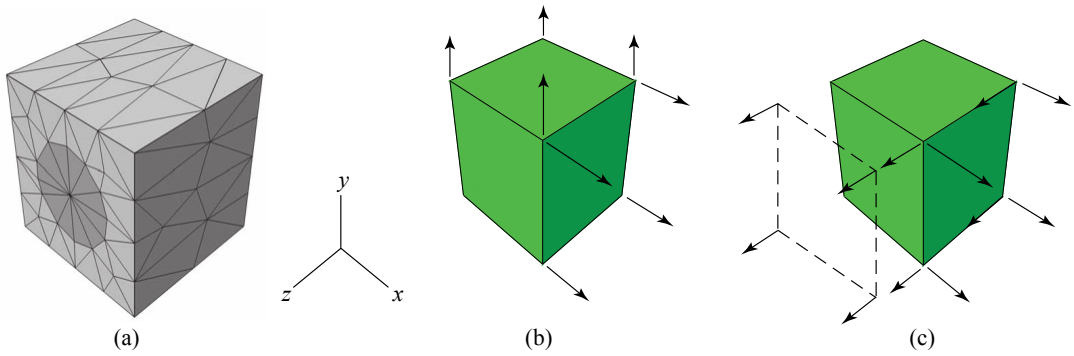

Figure 4.2: Geometry and discretization of the numerical example. (a) Microstructure; (b) Macrostructure subjected to biaxial tensile loading; (c) Macrostructure subjected to combined biaxial tensile and shear loading.

in Fig. 4.2 to determine the overlapping failure paths. Predictive failure models for this particular laminate will be of interest because multifaceted failure mechanisms can occur due to the complex interactions between the microconstituents. There are several different failure mechanisms which can occur as noted earlier. The investigation of these various failure modes will be extremely insightful and will provide predictive capabilities of how the particular microstructure will perform under these loading conditions. The understanding of these interactions will be key and it will be a challenge but a fun challenge none the less.

Exploration of the different mesh densities of the ROM must be taken into account, perhaps the microstructure consisting of 351 tetrahedra element is too coarse and a finer mesh will be needed. Failure paths in three-dimension are already complex, so having an extremely fine mesh will perhaps lead to more computational effort during the calculation of the nonlocal weights and the determination of failure paths.

Development of a reduced order model for laminated reinforced composite as shown in Fig. 4.1, will be investigated. In laminated composites, the plies are typically subjected to a combined state of normal stresses along the reinforcement and transverse directions as well as shear stresses that develop due to the mismatch between neighboring ply orientations. An in-depth assessment of the performance of the ROM will be investigated and compared

to the response of the direct numerical finite element analysis.

Appendix A

Details regarding damage model

To investigate the behavior of k in the damage model (i.e., Sparks model), a simple two-dimensional Mohrs Circle is drawn to show its geometric significance, for more information regarding the derivation of the modified principal strain definition details are given below.

From the numerical experiments it was observed that the material failure associated with the shearing strains failed at an axes that was not the principal axes, hence the need to modify the damage model to capture this effect. The model is limited to plane strain and it is assumed that the deformations occur within the planes, thus, $\varepsilon_{\mathbf{z}} = \gamma_{\mathbf{xz}} = \gamma_{\mathbf{yz}} = 0$. From any theory of elasticity book, when deriving the strain components, $\varepsilon_{\mathbf{x}}$, $\varepsilon_{\mathbf{y}}$, $\gamma_{\mathbf{xy}}$ and θ in terms of the reference $x'y'$ rotated through angle, θ, $\varepsilon_{\mathbf{x}'}$, $\varepsilon_{\mathbf{y}'}$, $\gamma_{\mathbf{x}'\mathbf{y}'}$ can be obtained. A square element is assumed with sides Δs, when the element is deformed then the respective sides are equal to $\Delta s(1+\varepsilon_x)$ and $\Delta s(1+\varepsilon_y)$, respectively and the angle formed is $\frac{\pi}{2} - \gamma_{xy}$ and $\frac{\pi}{2} + \gamma_{xy}$. The angles formed in the deformed configuration are assumed to be a function of a material parameter, k then the deformed angles that element make are $\frac{\pi}{2} - k\gamma_{xy}$ and $\frac{\pi}{2} + k\gamma_{xy}$. When k=1, then the general angles formed as a result of the deformation in the element are recovered. Utilizing the deformed element and applying algebraic and trigonometric identities, the expression below for the strain can be derived as,

$$\varepsilon(\theta) = \varepsilon_x \cos^2\theta + \varepsilon_y \sin^2\theta + k\gamma_{xy}\cos\theta\sin\theta \tag{A.1}$$

The main purpose of this section is to get an expression of the strain components in terms of the rotated frame of reference, thus below the equations are given

$$\varepsilon_{x'} = \frac{\varepsilon_{xx}+\varepsilon_{yy}}{2} + \frac{\varepsilon_{xx}-\varepsilon_{yy}}{2}\cos 2\theta + k\frac{\gamma_{xy}}{2}\sin 2\theta \tag{A.2}$$

$$\varepsilon_{y'} = \frac{\varepsilon_{xx}+\varepsilon_{yy}}{2} - \frac{\varepsilon_{xx}-\varepsilon_{yy}}{2}\cos 2\theta + k\frac{\gamma_{xy}}{2}\sin 2\theta \tag{A.3}$$

$$\frac{\gamma_{x'y'}}{2} = -(\frac{\varepsilon_{xx}-\varepsilon_{yy}}{2})\sin 2\theta + k\frac{\gamma_{xy}}{2}\cos 2\theta \tag{A.4}$$

The above equations may be written in a more succinct form which describes the modified plane strain transformation as shown below:

$$\varepsilon_{x',y'} = \frac{\varepsilon_{xx}+\varepsilon_{yy}}{2} \pm \sqrt{\left(\frac{\varepsilon_{xx}-\varepsilon_{yy}}{2}\right)^2 + (k\varepsilon_{xy})^2} \tag{A.5}$$

where $\frac{\gamma_{xy}}{2} = \varepsilon_{xy}$ and the modified angles from the principal orientations given as a function of the strain state:

$$\tan 2\theta' = \frac{2k\varepsilon_{xy}}{\varepsilon_{xx}-\varepsilon_{yy}} \tag{A.6}$$

$$\theta' = \frac{1}{2}\tan^{-1}\left(\frac{2k\varepsilon_{xy}}{\varepsilon_{xx}-\varepsilon_{yy}}\right) \tag{A.7}$$

The modified angles from the principal orientations given as a function of the strain state:

$$\theta' = \frac{1}{2}\tan^{-1}\left(\frac{2k\varepsilon_{xy}}{\varepsilon_{xx}-\varepsilon_{yy}}\right) \tag{A.8}$$

When exploring the effect of material parameter k on the model it is noted that there is a change in the Mohr's Circle and the corresponding axes of strain. When the use of $k \neq 1$, the equations for the transformation of plane strain are no longer representing the maximum and minimum normal and shearing strains and their corresponding principal orientations. Instead, according to Fig A.1, a reduction in the max in-plane strain state corresponding to a different orientation at an angle, α, from the principal orientation of θ_p is noticed. For a

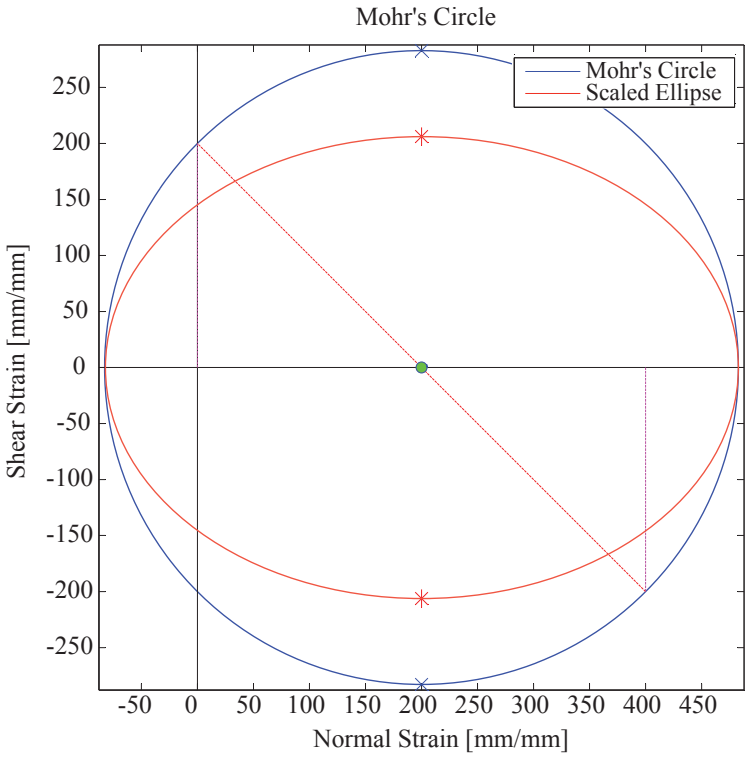

Figure A.1: Mohrs Circle with principal strains and scaled Mohrs Circle.

given strain state, $\varepsilon_x = 400\ \mu$, $\varepsilon_y = 0$, and $\gamma_{xy} = 200\ \mu$, the Mohr's Circle can be drawn as shown in Fig A.1. The blue line shows the original Mohr's Circle (when $k = 1$) and the red line shows (when $k \neq 1$) a reduction in the shear strain state and the Mohr's Circle exhibits an ellipse. This effect is evident when some experimental specimens are studied. When a specimen is loaded in shear, there is a reduction in the strength of the material and it fails before other specimens are loaded in a uniaxial fashion.

BIBLIOGRAPHY

[1] J. Fish, Q. Yu, and K. L. Shek. Computational damage mechanics for composite materials based on mathematical homogenization. *Int. J. Numer. Meth. Engng.*, 45:1657–1679, 1999.

[2] J. L. Chaboche, S. Kruch, J. F. Maire, and T. Pottier. Towards a micromechanics based inelastic and damage modeling of composites. *Int. J. Plasticity*, 17:411–439, 2001.

[3] J. C. Michel and P. Suquet. Computational analysis of nonlinear composite structures using the nonuniform transformation field analysis. *Comput. Meth. Appl. Mech. Engng*, 193:5477–5502, 2004.

[4] C. Oskay and J. Fish. Eigendeformation-based reduced order homogenization for failure analysis of heterogeneous materials. *Comp. Meth. Appl. Mech. Engng.*, 196:1216–1243, 2007.

[5] R. Crouch and C. Oskay. Symmetric meso-mechanical model for failure analysis of heterogeneous materials. *Int. J. Mult. Comp. Eng.*, 8:447–461, 2010.

[6] G. J. Dvorak. On uniform fields in heterogeneous media. *Proc. R. Soc. Lond. A*, 431:89–110, 1990.

[7] G. J. Dvorak. Transformation field analysis of inelastic composite materials. *Proc. R. Soc. Lond. A*, 437:311–327, 1992.

[8] W. W. Stinchcomb. Nondestructive evaluation of damage accumulation processes in composite laminates. *Compos. Sci. Technol.*, 25:103–118, 1986.

[9] A. de Moivre. *The doctrine of chances: or, a method of calculating the probability of events in play*. W. Pearson, 1718.

[10] D. da Silva. Proprietades geraes. *J. de l'Ecole Polytechnique*, I:cah.30, 1854.

[11] J. J. Sylvester. Note sur le theoreme de legendre cite dans une note inseree dans les comptes rendus. *C. R. Acad. Sci Paris*, 96:463–465, 1883.

[12] Filonova V. Fish, J. and Z. Yuan. Hybrid impotent-incompatible eigenstrain base homogenization. *Int. J. Numer. Meth. Engng.*, 95:1–32, 2013.

[13] I. Babuska. Homogenization and application. mathematical and computational problems. In B. Hubbard, editor, *Numerical Solution of Partial Differential Equations - III, SYNSPADE*. Academic Press, 1975.

[14] A. Benssousan, J. L. Lions, and G. Papanicolaou. *Asymptotic Analysis for Periodic Structures*. North-Holland, Amsterdam, 1978.

[15] P. M. Suquet. Elements of homogenization for inelastic solid mechanics. In E. Sanchez-Palencia and A. Zaoui, editors, *Homogenization Techniques for Composite Media*. Springer-Verlag, 1987.

[16] E. Sanchez-Palencia. *Non-homogeneous media and vibration theory*, volume 127 of *Lecture Notes in Physics*. Springer-Verlag, Berlin, 1980.

[17] J. Fish, K. L. Shek, M. Pandheeradi, and M. S. Shephard. Computational plasticity for composite structures based on mathematical homogenization: Theory and practice. *Comput. Meth. Appl. Mech. Engng.*, 148:53–73, 1997.

[18] F. V. Souza, D. H. Allen, and Y. Kim. Multiscale model for predicting damage evolution in composites due to impact loading. *Compos. Sci. Technol.*, 68:2624–2634, 2008.

[19] J. Fish and K. L. Shek. Finite deformation plasticity of composite structures: Computational models and adaptive strategies. *Comput. Meth. Appl. Mech. Engng.*, 172:145–174, 1999.

[20] V. Kouznetsova, M. G. D. Geers, and W. A. M. Brekelmans. Multi-scale constitutive modelling of heterogeneous materials with a gradient-enhanced computational homogenization scheme. *Int. J. Numer. Meth. Engng.*, 54:1235–1260, 2002.

[21] I. Ozdemir, W. A. M. Brekelmans, and M. G. D. Geers. Fe^2 computational homogenization for thermo-mechanical analysis of heterogeneous solids. *Comp. Meth. Appl. Mech. Engng.*, 198:602–613, 2008.

[22] K. Terada and Kurumatani M. Two-scale diffusion-deformation coupling model for material deterioration involving micro-crack propagation. *Int. J. Numer. Meth. Engng.*, 83:426–451, 2010.

[23] T. Massart, R. H. J. Peerlings, and M. G. D. Geers. Structural damage analysis of masonry walls using computational homogenization. *Int. J. Damage Mechanics*, 16:199–226, 2007.

[24] T. B. Belytschko, S. Loehnert, and J. H. Song. Multiscale aggregating discontinuities: a method for circumventing loss of material stability. *Int. J. Numer. Meth. Engng.*, 73:869–894, 2008.

[25] V. P. Nguyen, O. Lloberas-Valls, M. Stroeven, and L. J. Sluys. Computational homogenization for multiscale crack modeling implementational and computational aspects. *Int. J. Numer. Meth. Engng.*, 2011.

[26] F. Feyel and J.-L. Chaboche. Fe^2 multiscale approach for modelling the elastoviscoplastic behavior of long fiber sic/ti composite materials. *Comput. Methods Appl. Mech. Engrg.*, 183:309–330, 2000.

[27] Rahul and S. De. An efficient coarse-grained parallel algorithm for global-local multiscale computations on massively parallel systems. *Int. J. Numer. Meth. Engng.*, 82:379–402, 2010.

[28] C. Oskay. Two-level multiscale enrichment methodology for modeling of heterogeneous plates. *Int. J. Numer. Meth. Engng.*, 80:1143–1170, 2009.

[29] C. Oskay and G. Pal. A multiscale failure model for analysis of thin heterogeneous plates. *Int. J. Damage Mechanics*, 19:575–611, 2010.

[30] E. W. C. Coenen, V. G. Kouznetsova, and M. G. D. Geers. Computational homogenization for heterogeneous thin sheets. *Int. J. Numer. Meth. Engng.*, 83:1180–1205, 2010.

[31] B. Mercatoris and T. Massart. A coupled two-scale computational scheme for the failure of periodic quasi- brittle thin planar shells and its application to masonry. *Int. J. Numer. Meth. Engng.*, 85:1177–1206, 2011.

[32] S. Nemat-Nasser and M. Hori. *Micromechanics: Overall Properties of Heterogeneous Materials*. North-Holland, 1999.

[33] M. Gosz, B. Moran, and J. D. Achenbach. Matrix cracking in transversely loaded fiber composites with compliant interphases. In AMD-150/AD-32, editor, *Damage Mechanics in Composites*. ASME, 1992.

[34] S. Ghosh and S. Moorthy. Elastic-plastic analysis of arbitrary heterogeneous materials with the voronoi cell finite element method. *Comput. Methods Appl. Mech. Engng.*, 121:373–409, 1995.

[35] J. Aboudi. The generalized method of cells and high-fidelity generalized method of cells micromechanical models-a review. *Mech. Adv. Materials and Structures*, 11:329–366, 2005.

[36] H. Moulinec and P. Suquet. A numerical method for computing the overall response of nonlinear composites with complex microstructure. *Comput. Meth. Appl. Mech. Engng*, 157:69–94, 1998.

[37] L. V. Berlyand and A. G. Kolpakov. Network approximation in the limit of small interparticle distance of the effective properties of a high-contrast random dispersed composite. *Archive for Rational Mechanics and Analysis*, 159:179–227, 2001.

[38] J. Yvonnet and Q.-C. He. The reduced model multiscale method (R3M) for the non-linear homogenization of hyperelastic media at finite strains. *J. Comput. Phys.*, 223:341–368, 2007.

[39] H. Lamari, A. Ammar, P. Cartraud, G. Legrain, F. Chinesta, and F. Jacquemin. Routes for efficient computational homogenization of nonlinear materials using the proper generalized decompositions. *Arch. of Comput. Methods in Eng.*, 17:373–391, 2010.

[40] J. C. Simo and J. W. Ju. Strain- and stress-based continuum damage models - i. formulation. *Int. J. Solids Structures*, 23:821–840, 1987.

[41] J. Nocedal and S. Wright. *Numerical Optimization*. Springer Verlag, 2nd edition, 2006.

[42] J. H. Holland. *Adaptation in Natural and Artificial Systems*. University of Michigan Press, Ann Arbor, MI, USA, 1975.

[43] David E. Goldberg. *Genetic Algorithms in Search, Optimization, and Machine Learning*. Addison Wesley Longman, Inc., 1989.

[44] R. L. Haupt and S. E. Haupt. *Practical Genetic Algorithms*. Wiley-Interscience, 2004.

[45] Lawrence Davis. *Handbook of Genetic Algorithms*. Thomson Publishing Group / Van Nostrand Reinhold Company, New York, USA, 1991.

[46] B. Liu. *Two-level optimization of composite wing structures based on panel genetic optimization*. PhD thesis, University of Florida, 2001.

[47] *MathWorks: Genetic Algorithm Optimization Toolbox Users Guide, 2009*.

[48] R. Poli, W. B. Langdon, and N. F. McPhee. *A Field Guide to Genetic Programming*. Creative Commons Attribution-Noncommercial- No Derivative Works 2.0, United Kingdom, 2008.

[49] P. A. Sparks and C. Oskay. Calibration etc. *Int. J. Numer. Meth. Eng.*, pages 122–156, 2011.

[50] R. Furuhashi and T. Mura. On the equivalent inclusion method and impotent eigenstrains. *Journal of Elasticity*, 148:53–73, 1979.

[51] Paolo Giannozzi. Lecture notes: Numerical methods in quantum mechanics. Corso di Laurea Magistrale in Fisica; Anno accademico 2013/2014.

[52] Brown M. W. and Miller K. J. A theory for fatigue under multiaxial stress-strain conditions. *Proc. Inst. Mech. Engrs.*, 187:745–755, 1973.

[53] A. Fatemi and Socie D. F. A critical plane approach to multiaxial fatigue damage including out-of-phase loading. *Fatigue Fract. Mater. Struct.*, 11:3:149–165, 1988.

[54] Brown M. W. Kandil F. A. and Miller K. J. *Biaxial low cycle fatigue of 316 stainless steel at elevated tempertaures.* Metals Soc., London, 1982.

[55] Y. Liu and S. Mahadevan. Multiaxial high-cycle fatigue criterion and life prediction for metals. *International Journal of Fatigue*, 7:7:790–800, 2005.

[56] J. Mazar. *Application de la mecanique de lendommagement au comportement non lineaire et a la rupture du beton de structure*. PhD thesis, Universite Paris VI., France, 1984.

[57] Bazant Z. P. Pijaudier-Cabot, G. Nonlocal damage theory. *ASCE J. Eng. Mech*, 113:1512–1533, 1987.

[58] Z. P. Bazant and M. Jirasek. Nonlocal integral formulations of plasticity and damage: Survey of progress. *Journal of Engineering Mechanics*, 128:1119–1149, 2002.

[59] M. Jirasek. Non-local damage mechanics with application to concrete. *Failure, Degradation and Instabilities in Geomaterials*, pages 683–709, 2004.

[60] P. A. Sparks and C. Oskay. Identification of optimal reduced order homogenization models for failure of heterogeneous materials. *Journal for Multiscale Computational Engineering*, 11:185–200, 2013.